Geodesy and Geodynamics 14 (2023) 331–346

Contents lists available at ScienceDirect

Geodesy and Geodynamics

journal homepage: http://www.keaipublishing.com/geog

Fast 3D joint inversion of gravity and magnetic data based on cross gradient constraint

Sheng Liu [a], Xiangyun Wan [a], Shuanggen Jin [b, c, *], Bin Jia [a], Songbai Xuan [c], Quan Lou [a], Binbin Qin [a], Rongfu Peng [a], Dali Sun [d]

[a] Henan University of Urban Construction, Pingdingshan 467041, China
[b] School of Surveying and Land Information Engineering, Henan Polytechnic University, Jiaozuo 454000, China
[c] Shanghai Astronomical Observatory, Chinese Academy of Sciences, Shanghai 200030, China
[d] The First Monitoring and Application Center, China Earthquake Administration, Tianjin 300180, China

ARTICLE INFO

Article history:
Received 18 September 2022
Accepted 7 December 2022
Available online 27 January 2023

Keywords:
Gravity and magnetic data
Joint inversion
Triple
Cross-gradient constraint

ABSTRACT

The gravity and magnetic data can be adopted to interpret the internal structure of the Earth. To improve the calculation efficiency during the inversion process and the accuracy and reliability of the reconstructed physical property models, the triple strategy is adopted in this paper to develop a fast cross-gradient joint inversion for gravity and magnetic data. The cross-gradient constraint contains solving the gradients of the physical property models and performing the cross-product calculation of their gradients. The sparse matrices are first obtained by calculating the gradients of the physical property models derived from the first-order finite difference. Then, the triple method is applied to optimize the storages and the calculations related to the gradients of the physical property models. Therefore, the storage compression amount of the calculations related to the gradients of the physical property models and the cross-gradient constraint are reduced to one-fold of the number of grid cells at least, and the compression ratio increases with the increase of the number of grid cells. The test results from the synthetic data and field data prove that the structural coupling is achieved by using the fast cross-gradient joint inversion method to effectively reduce the multiplicity of solutions and improve the computing efficiency.

© 2023 Editorial office of Geodesy and Geodynamics. Publishing services by Elsevier B.V. on behalf of KeAi Communications Co. Ltd. This is an open access article under the CC BY-NC-ND license (http://creativecommons.org/licenses/by-nc-nd/4.0/).

1. Introduction

Geophysical inversion is a basic method for studying the crustal or lithospheric structure and evolution of the Earth. However, it is difficult for geophysical inversion to accurately determine the deep structures due to its inherent multiple solutions. Joint inversion of multiple geophysical data effectively reduces the problem of multiple solutions [1–4]. Currently, joint inversion methods can be divided into 2 categories. Firstly, the joint inversion is realized based on establishing the coupling relationship between different physical property parameters [5–12]. However, the geological conditions originating from different regions are different, and the corresponding empirical function relationship could be more consistent. Therefore, the joint inversions based on the empirical relationship of the physical property parameters contain certain limitations.

In general, the joint inversion methods for structural coupling constraints are based on different physical property models with the same structure. Gallardo and Meju [13,14] proposed a cross-gradient function to identify the boundaries of the same structures through the cross-product of the gradients of the different physical models, and conducted a two-dimensional cross-gradient joint inversion of seismic traveltime and DC resistivity data. Subsequently, Gallardo et al. [15] showed a joint inversion of the multi-physical parameters of the P-wave and S-wave, DC sounding and magnetic data in a region of Mexico. Gallardo et al. [16] once again conducted a multi-physical cross-gradient joint inversion of marine

* Corresponding author. School of Surveying and Land Information Engineering, Henan Polytechnic University, Jiaozuo 454000, China.
E-mail addresses: 1500240410@qq.com (S. Liu), xywan51@126.com (X. Wan), sgjin@shao.ac.cn (S. Jin), jia_yang1101@163.com (B. Jia), sbxuan@shao.ac.cn (S. Xuan), 20191009@hncj.edu.cn (Q. Lou), qinbinlj@126.com (B. Qin), 20172056@hncj.edu.cn (R. Peng), 574111077@qq.com (D. Sun).

Peer review under responsibility of Institute of Seismology, China Earthquake Administration.

Production and Hosting by Elsevier on behalf of KeAi

https://doi.org/10.1016/j.geog.2022.12.003
1674-9847/© 2023 Editorial office of Geodesy and Geodynamics. Publishing services by Elsevier B.V. on behalf of KeAi Communications Co. Ltd. This is an open access article under the CC BY-NC-ND license (http://creativecommons.org/licenses/by-nc-nd/4.0/).

seismic reflection, marine magnetotelluric, gravity and magnetic data on a long profile in a region of Brazil. Currently, the cross-gradient joint inversion method has been widely adopted in the joint inversion of geophysical data [17–21].

However, computational efficiency consistently restricts the development of the application of field data inversion. From the perspective of joint inversion of gravity and magnetic data, this paper intends to develop an efficient method for deep structure detection to meet the needs of efficient computing. Generally, the cross-gradient joint inversion requires the cross-product calculation of the gradients of the physical property models, and the models' gradients are typical sparse matrices. Therefore, computation directly on large sparse matrices will consume a lot of computing resources and calculation time. Consequently, optimizing the estimation of sparse matrices with suitable strategies for reducing computing cost is momentous. In this paper, based on the sparse matrices' storage and operation strategy of triplet, a fast cross-gradient joint inversion method for field data is proposed to reduce the computing cost and improve the inversion accuracy. The conjugate gradient method is adopted to the calculations of the joint inversion. Additionally, synthetic data and field data are employed to validate the correctness and effectiveness of the developed algorithm in this paper.

2. Methodology

2.1. Cross gradient constraint

Generally, the magnitude of the cross-gradient vector obtained by the cross product of the gradient vectors of the density model and magnetization model can reflect the structural similarity of the two physical property models. Generally, the cross-gradient vector can be expressed as the following formula.

$$\begin{aligned}\boldsymbol{t}=(\boldsymbol{t}_x,\boldsymbol{t}_y,\boldsymbol{t}_z)=\nabla\boldsymbol{m}_1\times\nabla\boldsymbol{m}_2=&\begin{vmatrix}\boldsymbol{i}&\boldsymbol{j}&\boldsymbol{k}\\ \nabla\boldsymbol{m}_1^x&\nabla\boldsymbol{m}_1^y&\nabla\boldsymbol{m}_1^z\\ \nabla\boldsymbol{m}_2^x&\nabla\boldsymbol{m}_2^y&\nabla\boldsymbol{m}_2^z\end{vmatrix}\\ =&\left(\nabla\boldsymbol{m}_1^y\nabla\boldsymbol{m}_2^z-\nabla\boldsymbol{m}_1^z\nabla\boldsymbol{m}_2^y,\nabla\boldsymbol{m}_1^z\nabla\boldsymbol{m}_2^x\right.\\ &\left.-\nabla\boldsymbol{m}_1^x\nabla\boldsymbol{m}_2^z,\nabla\boldsymbol{m}_1^x\nabla\boldsymbol{m}_2^y-\nabla\boldsymbol{m}_1^y\nabla\boldsymbol{m}_2^x\right)\end{aligned}\tag{1}$$

For a single meshing cell, $\boldsymbol{t}=(\boldsymbol{t}_x,\boldsymbol{t}_y,\boldsymbol{t}_z)$ represents the cross-gradient vector of the 2 physical property models in the x, y and z direction. For the all underground grid cells, $\boldsymbol{t}$ represents a matrix of order $N\times 3$, and N is the number of the volume pixels. Its i_{th} rows represent the cross-gradient vectors of the two models at i_{th} unit. $\boldsymbol{i}$, $\boldsymbol{j}$ and $\boldsymbol{k}$ represent unit vectors in the x, y and z directions, respectively. $\boldsymbol{m}_1$ and $\boldsymbol{m}_2$ represent the density model and the magnetization model, respectively. $\nabla\boldsymbol{m}_1=\nabla\boldsymbol{m}_1^x\boldsymbol{i}+\nabla\boldsymbol{m}_1^y\boldsymbol{j}+\nabla\boldsymbol{m}_1^z\boldsymbol{k}$ and $\nabla\boldsymbol{m}_2=\nabla\boldsymbol{m}_2^x\boldsymbol{i}+\nabla\boldsymbol{m}_2^y\boldsymbol{j}+\nabla\boldsymbol{m}_2^z\boldsymbol{k}$ represent the gradient vectors of the density model and the magnetization model, respectively. In Eq. (1), $\nabla\boldsymbol{m}_1^x$, $\nabla\boldsymbol{m}_1^y$ and $\nabla\boldsymbol{m}_1^z$ represent the gradient matrix of the density model $\boldsymbol{m}_1$ in the x, y and z directions, respectively, and $\nabla\boldsymbol{m}_2^x$, $\nabla\boldsymbol{m}_2^y$ and $\nabla\boldsymbol{m}_2^z$ represent the gradient matrix of the magnetization model in the x, y and z direction, respectively. In this paper, the forward difference method is adopted to calculate the gradients of the density model and magnetization model. Fig. 1 represent a schematic diagram for forward differential processing of the physical property models.

Then, the 3 components of the cross-gradient operator of the density model and magnetization model can be transformed as the following formulas.

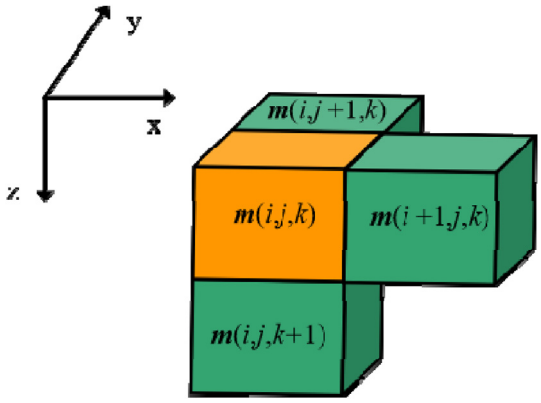

Fig. 1. A schematic diagram of a three-dimensional discrete process for forward differential processing.

$$\begin{cases}\boldsymbol{t}_x=\nabla\boldsymbol{m}_2^y\nabla\boldsymbol{m}_1^z-\nabla\boldsymbol{m}_2^z\nabla\boldsymbol{m}_1^y=\boldsymbol{D}_y\boldsymbol{m}_2\boldsymbol{D}_z\boldsymbol{m}_1-\boldsymbol{D}_z\boldsymbol{m}_2\boldsymbol{D}_y\boldsymbol{m}_1\\ \quad=(\boldsymbol{D}_y\boldsymbol{m}_2\boldsymbol{D}_z-\boldsymbol{D}_z\boldsymbol{m}_2\boldsymbol{D}_y)\boldsymbol{m}_1=\boldsymbol{B}\boldsymbol{x}_1\boldsymbol{m}_1\\ \boldsymbol{t}_y=\nabla\boldsymbol{m}_2^z\nabla\boldsymbol{m}_1^x-\nabla\boldsymbol{m}_2^x\nabla\boldsymbol{m}_1^z=\boldsymbol{D}_z\boldsymbol{m}_2\boldsymbol{D}_x\boldsymbol{m}_1-\boldsymbol{D}_x\boldsymbol{m}_2\boldsymbol{D}_z\boldsymbol{m}_1\\ \quad=(\boldsymbol{D}_z\boldsymbol{m}_2\boldsymbol{D}_x-\boldsymbol{D}_x\boldsymbol{m}_2\boldsymbol{D}_z)\boldsymbol{m}_1=\boldsymbol{B}\boldsymbol{y}_1\boldsymbol{m}_1\\ \boldsymbol{t}_z=\nabla\boldsymbol{m}_2^x\nabla\boldsymbol{m}_1^y-\nabla\boldsymbol{m}_2^y\nabla\boldsymbol{m}_1^x=\boldsymbol{D}_x\boldsymbol{m}_2\boldsymbol{D}_y\boldsymbol{m}_1-\boldsymbol{D}_y\boldsymbol{m}_2\boldsymbol{D}_x\boldsymbol{m}_1\\ \quad=(\boldsymbol{D}_x\boldsymbol{m}_2\boldsymbol{D}_y-\boldsymbol{D}_y\boldsymbol{m}_2\boldsymbol{D}_x)\boldsymbol{m}_1=\boldsymbol{B}\boldsymbol{z}_1\boldsymbol{m}_1\end{cases}\tag{2}$$

where $\boldsymbol{D}_x$, $\boldsymbol{D}_y$ and $\boldsymbol{D}_z$ are the first-order forward difference operators in x, y and z direction, respectively. Based on Eqs. (1) and (2), the cross-gradient constraint $\Phi_{\text{cross}}(\boldsymbol{m}_1,\boldsymbol{m}_2)$ can be expressed as the following formula.

$$\begin{aligned}\Phi_{\text{cross}}(\boldsymbol{m}_1,\boldsymbol{m}_2)=\|\boldsymbol{t}\|_2^2=&\boldsymbol{t}_{\boldsymbol{x}}^{\mathrm{T}}\boldsymbol{t}_{\boldsymbol{x}}+\boldsymbol{t}_{\boldsymbol{y}}^{\mathrm{T}}\boldsymbol{t}_{\boldsymbol{y}}+\boldsymbol{t}_{\boldsymbol{z}}^{\mathrm{T}}\boldsymbol{t}_{\boldsymbol{z}}\\ =&(\boldsymbol{B}\boldsymbol{x}_1\boldsymbol{m}_1)^{\mathrm{T}}(\boldsymbol{B}\boldsymbol{x}_1\boldsymbol{m}_1)+(\boldsymbol{B}\boldsymbol{y}_1\boldsymbol{m}_1)^{\mathrm{T}}(\boldsymbol{B}\boldsymbol{y}_1\boldsymbol{m}_1)\\ &+(\boldsymbol{B}\boldsymbol{z}_1\boldsymbol{m}_1)^{\mathrm{T}}(\boldsymbol{B}\boldsymbol{z}_1\boldsymbol{m}_1)\end{aligned}\tag{3}$$

Generally, the structure similarity of different physical property models defined by the cross-gradient vector $\boldsymbol{t}$ contains two different cases. The first case represent that the 2 physical property models change simultaneously in the same or the opposite direction at the same position. The second case represent that the parameter in a physical property model remains constant, while the parameter of the other physical property model arbitrarily changes at the same position. Therefore, when the value of the cross-gradient vector $\boldsymbol{t}$ is equal to 0, it means that the structures of the density model and the magnetization model at the corresponding positions are similar.

2.2. Cross-gradient joint inversion method

Generally, the objective function of the cross-gradient joint inversion of geophysical data includes data constraint, model constraint and cross-gradient constraint [13,14], which can be expressed as the following formula,

$$\begin{aligned}\Phi(\boldsymbol{m}_1,\boldsymbol{m}_2)=&\mu_1\Phi_{\boldsymbol{d}_1}(\boldsymbol{m}_1)+\beta_1\Phi_{\boldsymbol{m}_1}(\boldsymbol{m}_1)+\mu_2\Phi_{\boldsymbol{d}_2}(\boldsymbol{m}_2)\\ &+\beta_2\Phi_{\boldsymbol{m}_2}(\boldsymbol{m}_2)+\lambda\Phi_{\text{cross}}(\boldsymbol{m}_1,\boldsymbol{m}_2)\\ =&\mu_1\|\boldsymbol{G}_1\boldsymbol{m}_1-\boldsymbol{d}_1\|_2^2+\beta_1\left\|\boldsymbol{w}_1\left(\boldsymbol{m}_1-\boldsymbol{m}_1^{\text{ref}}\right)\right\|_2^2\\ &+\mu_2\|\boldsymbol{G}_2\boldsymbol{m}_2-\boldsymbol{d}_2\|_2^2+\beta_2\left\|\boldsymbol{w}_2\left(\boldsymbol{m}_2-\boldsymbol{m}_2^{\text{ref}}\right)\right\|_2^2\\ &+\lambda\Phi_{\text{cross}}(\boldsymbol{m}_1,\boldsymbol{m}_2)\end{aligned}\tag{4}$$

where Φ represents the objective function of the cross-gradient joint inversion; $\Phi_{\boldsymbol{d}_1}$ and $\Phi_{\boldsymbol{d}_2}$ represent data constraints of gravity and magnetic data, respectively; $\Phi_{\boldsymbol{m}_1}$ and $\Phi_{\boldsymbol{m}_2}$ represent model constraints of gravity and magnetic data, respectively; $\boldsymbol{d}_1$ and $\boldsymbol{d}_2$ represent the observed gravity data and magnetic data, respectively; $\boldsymbol{G}_1$ and $\boldsymbol{G}_2$ represent the forward response of the density model and magnetization model, respectively; $\boldsymbol{m}_1^{\mathrm{ref}}$ and $\boldsymbol{m}_2^{\mathrm{ref}}$ represent the reference density model and reference magnetization model, respectively; μ_1 and μ_2 represent the weighting parameters of the gravity and magnetic data constraints, respectively; β_1 and β_2 represent the regularization parameters of gravity and magnetic data, respectively, and λ represents the weighting parameter of the cross-gradient constraint. $\boldsymbol{w}_1$ represents the result of $\boldsymbol{w}_{\boldsymbol{m}_1}$ multiplied the depth weighted matrix [22,23], $\boldsymbol{w}_{\boldsymbol{m}_1} = [(1-\tau_1)(\boldsymbol{m}_1^2+\varepsilon^2)^{-1/2}+\tau_1\boldsymbol{I}]^{1/2}$ [24], $\boldsymbol{I}$ represents the identity matrix, ε represents a small non negative value, τ_1 ranges from 0 to 1.0 and $\boldsymbol{w}_2$ contain the similar form of $\boldsymbol{w}_1$.

The strategy of alternating iterations [18] can be adopted to avoid the choice of parameters μ_1 and μ_2, and then the objective function of the cross-gradient joint inversion can be transformed as the following formulas.

$$\begin{cases} \Phi_1(\boldsymbol{m}_1,\boldsymbol{m}_2) = \Phi_{\boldsymbol{d}_1}(\boldsymbol{m}_1)+\beta_1\Phi_{\boldsymbol{m}_1}(\boldsymbol{m}_1)+\lambda_1\Phi_{\mathrm{cross}}(\boldsymbol{m}_1,\boldsymbol{m}_2) \\ = \|\boldsymbol{G}_1\boldsymbol{m}_1-\boldsymbol{d}_1\|_2^2+\beta_1\left\|\boldsymbol{w}_1\left(\boldsymbol{m}_1-\boldsymbol{m}_1^{\mathrm{ref}}\right)\right\|_2^2+\lambda_1\Phi_{\mathrm{cross}}(\boldsymbol{m}_1,\boldsymbol{m}_2) \\ \Phi_2(\boldsymbol{m}_1,\boldsymbol{m}_2) = \Phi_{\boldsymbol{d}_2}(\boldsymbol{m}_2)+\beta_2\Phi_{\boldsymbol{m}_2}(\boldsymbol{m}_2)+\lambda_2\Phi_{\mathrm{cross}}(\boldsymbol{m}_1,\boldsymbol{m}_2) \\ = \|\boldsymbol{G}_2\boldsymbol{m}_2-\boldsymbol{d}_2\|_2^2+\beta_2\left\|\boldsymbol{w}_2\left(\boldsymbol{m}_2-\boldsymbol{m}_2^{\mathrm{ref}}\right)\right\|_2^2+\lambda_2\Phi_{\mathrm{cross}}(\boldsymbol{m}_1,\boldsymbol{m}_2) \end{cases} \tag{5}$$

where λ_1 and λ_2 represent the weighting parameters of the cross-gradient constraint for gravity and magnetic data, respectively. The conjugate gradient algorithm is adopted to solve the objective function of the cross-gradient joint inversion, and the gradients of the objective function needs to be calculated. After taking the derivatives of Eq. (5) for density model $\boldsymbol{m}_1$ and magnetization model $\boldsymbol{m}_2$, respectively, the following equation can be obtained.

$$\begin{cases} \dfrac{\partial\Phi_1}{\partial\boldsymbol{m}_1} = \boldsymbol{G}_1^{\mathrm{T}}\boldsymbol{G}_1\boldsymbol{m}_1+\beta_1\boldsymbol{w}_1^{\mathrm{T}}\boldsymbol{w}_1\boldsymbol{m}_1 \\ \qquad +\lambda_1\left[\boldsymbol{Bx}_1^{\mathrm{T}}\boldsymbol{Bx}_1\boldsymbol{m}_1+\boldsymbol{By}_1^{\mathrm{T}}\boldsymbol{By}_1\boldsymbol{m}_1+\boldsymbol{Bz}_1^{\mathrm{T}}\boldsymbol{Bz}_1\boldsymbol{m}_1\right] \\ \qquad -\boldsymbol{G}_1^{\mathrm{T}}\boldsymbol{d}_1-\beta_1\boldsymbol{w}_1^{\mathrm{T}}\boldsymbol{w}_1\boldsymbol{m}_1^{\mathrm{ref}} \\ \dfrac{\partial\Phi_2}{\partial\boldsymbol{m}_2} = \boldsymbol{G}_2^{\mathrm{T}}\boldsymbol{G}_2\boldsymbol{m}_2+\beta_2\boldsymbol{w}_2^{\mathrm{T}}\boldsymbol{w}_2\boldsymbol{m}_2 \\ \qquad +\lambda_2\left[\boldsymbol{Bx}_2^{\mathrm{T}}\boldsymbol{Bx}_2\boldsymbol{m}_2+\boldsymbol{By}_2^{\mathrm{T}}\boldsymbol{By}_2\boldsymbol{m}_2+\boldsymbol{Bz}_2^{\mathrm{T}}\boldsymbol{Bz}_2\boldsymbol{m}_2\right] \\ \qquad -\boldsymbol{G}_2^{\mathrm{T}}\boldsymbol{d}_2-\beta_2\boldsymbol{w}_2^{\mathrm{T}}\boldsymbol{w}_2\boldsymbol{m}_2^{\mathrm{ref}} \end{cases} \tag{6}$$

In the inversion of field data, the model weighting and reweighting strategies can improve the resolution of the recovered models and speed up the convergence efficiency. Let $\boldsymbol{m}_1^{\mathrm{w}} = \boldsymbol{w}_1\boldsymbol{m}_1$, $\boldsymbol{m}_2^{\mathrm{w}} = \boldsymbol{w}_2\boldsymbol{m}_2$, $\boldsymbol{m}_1^{\mathrm{ref(w)}} = \boldsymbol{w}_1\boldsymbol{m}_1^{\mathrm{ref}}$, $\boldsymbol{m}_2^{\mathrm{ref(w)}} = \boldsymbol{w}_2\boldsymbol{m}_2^{\mathrm{ref}}$, $\boldsymbol{G}_1^{\mathrm{w}} = \boldsymbol{G}_1\boldsymbol{w}_1{}^{-1}$, $\boldsymbol{G}_2^{\mathrm{w}} = \boldsymbol{G}_2\boldsymbol{w}_2{}^{-1}$, $\boldsymbol{Bx}_1^{\mathrm{w}} = \boldsymbol{Bx}_1\boldsymbol{w}_1^{-1}$, $\boldsymbol{By}_1^{\mathrm{w}} = \boldsymbol{By}_1\boldsymbol{w}_1^{-1}$, $\boldsymbol{Bz}_1^{\mathrm{w}} = \boldsymbol{Bz}_1\boldsymbol{w}_1^{-1}$, $\boldsymbol{Bx}_2^{\mathrm{w}} = \boldsymbol{Bx}_2\boldsymbol{w}_2^{-1}$, $\boldsymbol{By}_2^{\mathrm{w}} = \boldsymbol{By}_2\boldsymbol{w}_2^{-1}$ and $\boldsymbol{Bz}_2^{\mathrm{w}} = \boldsymbol{Bz}_2\boldsymbol{w}_2^{-1}$. Eq. (5) can be transformed as the following formulas.

$$\begin{cases} \Phi_1(\boldsymbol{m}_1^{\mathrm{w}},\boldsymbol{m}_2^{\mathrm{w}}) = \Phi_{\boldsymbol{d}_1}(\boldsymbol{m}_1^{\mathrm{w}})+\beta_1\Phi_{\boldsymbol{m}_1^{\mathrm{w}}}(\boldsymbol{m}_1^{\mathrm{w}})+\lambda_1\Phi_{\mathrm{cross}}(\boldsymbol{m}_1^{\mathrm{w}},\boldsymbol{m}_2^{\mathrm{w}}) \\ \Phi_2(\boldsymbol{m}_1^{\mathrm{w}},\boldsymbol{m}_2^{\mathrm{w}}) = \Phi_{\boldsymbol{d}_2}(\boldsymbol{m}_2^{\mathrm{w}})+\beta_2\Phi_{\boldsymbol{m}_2^{\mathrm{w}}}(\boldsymbol{m}_2^{\mathrm{w}})+\lambda_2\Phi_{\mathrm{cross}}(\boldsymbol{m}_1^{\mathrm{w}},\boldsymbol{m}_2^{\mathrm{w}}) \end{cases} \tag{7}$$

From Eq. (7), the following Eq. (8) can be acquired.

$$\begin{cases} \dfrac{\partial\Phi_1}{\partial\boldsymbol{m}_1^{\mathrm{w}}} = \boldsymbol{G}_1^{\mathrm{wT}}\boldsymbol{G}_1^{\mathrm{w}}\boldsymbol{m}_1^{\mathrm{w}}+\beta_1\boldsymbol{m}_1^{\mathrm{w}} \\ \qquad +\lambda_1\left[(\boldsymbol{Bx}_1^{\mathrm{w}})^{\mathrm{T}}\boldsymbol{Bx}_1^{\mathrm{w}}\boldsymbol{m}_1^{\mathrm{w}}+(\boldsymbol{By}_1^{\mathrm{w}})^{\mathrm{T}}\boldsymbol{By}_1^{\mathrm{w}}\boldsymbol{m}_1^{\mathrm{w}}+(\boldsymbol{Bz}_1^{\mathrm{w}})^{\mathrm{T}}\boldsymbol{Bz}_1^{\mathrm{w}}\boldsymbol{m}_1^{\mathrm{w}}\right] \\ \qquad -\boldsymbol{G}_1^{\mathrm{wT}}\boldsymbol{d}_1-\beta_1\boldsymbol{m}_1^{\mathrm{ref(w)}} \\ \dfrac{\partial\Phi_2}{\partial\boldsymbol{m}_2^{\mathrm{w}}} = \boldsymbol{G}_2^{\mathrm{wT}}\boldsymbol{G}_2^{\mathrm{w}}\boldsymbol{m}_2^{\mathrm{w}}+\beta_2\boldsymbol{m}_2^{\mathrm{w}} \\ \qquad +\lambda_2\left[(\boldsymbol{Bx}_2^{\mathrm{w}})^{\mathrm{T}}\boldsymbol{Bx}_2^{\mathrm{w}}\boldsymbol{m}_2^{\mathrm{w}}+(\boldsymbol{By}_2^{\mathrm{w}})^{\mathrm{T}}\boldsymbol{By}_2^{\mathrm{w}}\boldsymbol{m}_2^{\mathrm{w}}+(\boldsymbol{Bz}_2^{\mathrm{w}})^{\mathrm{T}}\boldsymbol{Bz}_2^{\mathrm{w}}\boldsymbol{m}_2^{\mathrm{w}}\right] \\ \qquad -\boldsymbol{G}_2^{\mathrm{wT}}\boldsymbol{d}_2-\beta_2\boldsymbol{m}_2^{\mathrm{ref(w)}} \end{cases} \tag{8}$$

In this paper, the elastic-net regularization constraint is adopted to the model constraint [24,25] and the reference models are all zero values.

2.3. Fast cross-gradient joint inversion method

The forward difference method is adopted for calculating the gradients of the physical property models, and each row of the matrices of the gradients has only 2 non-zero elements. $\boldsymbol{D}_x$, $\boldsymbol{D}_y$ and $\boldsymbol{D}_z$ are the finite difference matrices in the x, y and z directions, respectively, and those matrices are sparse matrices of dimension $N \times N$. The dimensions of the finite difference matrices will be increased with the increasing number of volume pixels. The calculation of the cross-gradient constraint and its gradient involves finite difference matrices. When computing them directly, it will consume a lot of memory and time. The triple method is adopted to store and operate the sparse matrices, which only need to store the number of rows, columns and element values of the non-zero elements of the sparse matrices. Therefore, the triple method is adopted to compute and store sparse matrices to implement a fast cross-gradient joint inversion method in this paper.

Firstly, the storage and computation of $\boldsymbol{D}_x$, $\boldsymbol{D}_y$ and $\boldsymbol{D}_z$ will be optimized. The forward difference matrix $\boldsymbol{D}_x\begin{bmatrix} -1 & 1 & \cdots & 0 \\ 0 & -1 & 1\cdots & 0 \\ \vdots & \vdots & \ddots & \vdots \\ 0 & 0 & \cdots & 0 \end{bmatrix}_{N\times N}$ can be expressed as $\begin{bmatrix} 1 & 1 & -1 \\ 1 & 2 & 1 \\ \vdots & \vdots & \vdots \end{bmatrix}_{2N\times 3}$ based on the triple method. The 3 elements of each row in the $\boldsymbol{D}_x$ are the row number, column number, element value of the non-zero element, and then the data in the third column is divided by the step size dx, which is the subdivision unit in the x direction. A triple matrix stores all non-zero elements sequentially in row-major order. In a similar way, $\boldsymbol{D}_y\begin{bmatrix} -1 & \cdots & 1 & \cdots & 0 \\ 0 & -1 & \cdots & 1\cdots & 0 \\ \vdots & \vdots & \cdots & \ddots & \vdots \\ 0 & 0 & \cdots & 0 & 0 \end{bmatrix}_{N\times N}$ can be transformed to $\begin{bmatrix} 1 & 1 & 1 \\ 1 & 1+N_{\mathrm{col}} & -1 \\ \vdots & \vdots & \vdots \end{bmatrix}_{2N\times 3}$ and $\boldsymbol{D}_z\begin{bmatrix} -1 & \cdots & \cdots & 1 & \cdots & 0 \\ 0 & -1 & \cdots & \cdots & 1\cdots & 0 \\ \vdots & \vdots & \cdots & \cdots & \ddots & \vdots \\ 0 & 0 & \cdots & \cdots & 0 & 0 \end{bmatrix}_{N\times N}$ can be transformed to $\begin{bmatrix} 1 & 1 & 1 \\ 1 & 1+N_{\mathrm{row}}\times N_{\mathrm{col}} & -1 \\ \vdots & \vdots & \vdots \end{bmatrix}_{2N\times 3}$, where N_{col}

and N_{row} represent the numbers of meshing units in the x and y direction, and then the data in the third column of $\boldsymbol{D}_y$ and $\boldsymbol{D}_z$ are divided by the step size dy in the y direction and dz in the z direction, respectively. It can be found that the storage capacity of the $\boldsymbol{D}_x$, $\boldsymbol{D}_y$ and $\boldsymbol{D}_z$ are reduced from $N \times N$ to $2 \times N \times 3$, which presents that the magnitude of the calculation amount is reduced to the $1/N$ of that of the original method.

Secondly, the storage and calculation of the cross-gradient matrices $\boldsymbol{Bx}_1$, $\boldsymbol{By}_1$ and $\boldsymbol{Bz}_1$ are optimized.

$$\begin{cases} \boldsymbol{Bx}_1 = \boldsymbol{D}_y(\boldsymbol{D}_z\boldsymbol{m}_2) - \boldsymbol{D}_z(\boldsymbol{D}_y\boldsymbol{m}_2) \\ \boldsymbol{By}_1 = \boldsymbol{D}_z(\boldsymbol{D}_x\boldsymbol{m}_2) - \boldsymbol{D}_x(\boldsymbol{D}_z\boldsymbol{m}_2) \\ \boldsymbol{Bz}_1 = \boldsymbol{D}_x(\boldsymbol{D}_y\boldsymbol{m}_2) - \boldsymbol{D}_y(\boldsymbol{D}_x\boldsymbol{m}_2) \end{cases} \tag{9}$$

In Eq. (9), the calculation of $\boldsymbol{Bx}_1$ is divided into 2 parts $\boldsymbol{Bx}_1^1$ and $\boldsymbol{Bx}_1^2$ ($\boldsymbol{Bx}_1^1 = \boldsymbol{D}_y(\boldsymbol{D}_z\boldsymbol{m}_2)$, $\boldsymbol{Bx}_1^2 = \boldsymbol{D}_z(\boldsymbol{D}_y\boldsymbol{m}_2)$). Then, the calculation of $\boldsymbol{Bx}_1^1$ is also divided into 2 steps, the first step has the following form.

$$\boldsymbol{D}_z\boldsymbol{m}_2 = \begin{bmatrix} & & & \\ 1 & 1 & -1/\mathrm{d}z & \\ 1 & 1+N_{\mathrm{row}}\times N_{\mathrm{col}} & 1/\mathrm{d}z & \\ 2 & 2 & -1/\mathrm{d}z & \\ 2 & 2+N_{\mathrm{row}}\times N_{\mathrm{col}} & 1/\mathrm{d}z & \\ \vdots & \vdots & & \vdots \end{bmatrix}_{2N\times 3} \begin{bmatrix} \boldsymbol{m}_2^1 \\ \boldsymbol{m}_2^2 \\ \boldsymbol{m}_2^3 \\ \boldsymbol{m}_2^4 \\ \vdots \end{bmatrix}_{N\times 1}$$
$$= \begin{bmatrix} -1/\mathrm{d}z \times \boldsymbol{m}_2^1 + 1/\mathrm{d}z \times \boldsymbol{m}_2^{1+N_{\mathrm{row}}\times N_{\mathrm{col}}} \\ -1/\mathrm{d}z \times \boldsymbol{m}_2^2 + 1/\mathrm{d}z \times \boldsymbol{m}_2^{2+N_{\mathrm{row}}\times N_{\mathrm{col}}} \\ \vdots \end{bmatrix}_{N\times 1} = \begin{bmatrix} Z_1^1 \\ Z_1^2 \\ \vdots \end{bmatrix}_{N\times 1}$$

The second step can be expressed as the following form.

$$\boldsymbol{Bx}_1^1 = \boldsymbol{D}_y \begin{bmatrix} Z_1^1 \\ Z_1^2 \\ \vdots \end{bmatrix}_{N\times 1} = \begin{bmatrix} 1 & 1 & -1/\mathrm{d}y & \\ 1 & 1+N_{\mathrm{col}} & 1/\mathrm{d}y & \\ 2 & 2 & -1/\mathrm{d}y & \\ 2 & 2+N_{\mathrm{col}} & 1/\mathrm{d}y & \\ \vdots & \vdots & & \vdots \end{bmatrix}_{2N\times 3} \begin{bmatrix} Z_1^1 \\ Z_1^2 \\ \vdots \end{bmatrix}_{N\times 1}$$
$$= \begin{bmatrix} 1 & 1 & -1/\mathrm{d}y \times Z_1^1 & \\ 1 & 1+N_{\mathrm{col}} & 1/\mathrm{d}y \times Z_1^1 & \\ 2 & 2 & -1/\mathrm{d}y \times Z_1^2 & \\ 2 & 2+N_{\mathrm{col}} & 1/\mathrm{d}y \times Z_1^2 & \\ \vdots & \vdots & & \vdots \end{bmatrix}_{2N\times 3}$$

Then, the calculation of $\boldsymbol{Bx}_1^2$ is also divided into 2 steps

$$\boldsymbol{D}_y\boldsymbol{m}_2 = \begin{bmatrix} 1 & 1 & -1/\mathrm{d}y & \\ 1 & 1+N_{\mathrm{col}} & 1/\mathrm{d}y & \\ 2 & 2 & -1/\mathrm{d}y & \\ 2 & 2+N_{\mathrm{col}} & 1/\mathrm{d}y & \\ \vdots & \vdots & & \vdots \end{bmatrix}_{2N\times 3} \begin{bmatrix} \boldsymbol{m}_2^1 \\ \boldsymbol{m}_2^2 \\ \boldsymbol{m}_2^3 \\ \boldsymbol{m}_2^4 \\ \vdots \end{bmatrix}_{N\times 1}$$
$$= \begin{bmatrix} -1/\mathrm{d}y \times \boldsymbol{m}_2^1 + 1/\mathrm{d}y \times \boldsymbol{m}_2^{1+N_{\mathrm{col}}} \\ -1/\mathrm{d}y \times \boldsymbol{m}_2^2 + 1/\mathrm{d}y \times \boldsymbol{m}_2^{2+N_{\mathrm{col}}} \\ \vdots \end{bmatrix}_{N\times 1} = \begin{bmatrix} Y_1^1 \\ Y_1^2 \\ \vdots \end{bmatrix}_{N\times 1}$$

and

$$\boldsymbol{Bx}_1^2 = \boldsymbol{D}_z \begin{bmatrix} Y_1^1 \\ Y_1^2 \\ \vdots \end{bmatrix}_{N\times 1} = \begin{bmatrix} & & & \\ 1 & 1 & -1/\mathrm{d}z & \\ 1 & 1+N_{\mathrm{row}}\times N_{\mathrm{col}} & 1/\mathrm{d}z & \\ 2 & 2 & -1/\mathrm{d}z & \\ 2 & 2+N_{\mathrm{row}}\times N_{\mathrm{col}} & 1/\mathrm{d}z & \\ \vdots & \vdots & & \vdots \end{bmatrix}_{2N\times 3} \begin{bmatrix} Y_1^1 \\ Y_1^2 \\ \vdots \end{bmatrix}_{N\times 1}$$
$$= \begin{bmatrix} 1 & 1 & -1/\mathrm{d}z \times Y_1^1 & \\ 1 & 1+N_{\mathrm{row}}\times N_{\mathrm{col}} & 1/\mathrm{d}z \times Y_1^1 & \\ 2 & 2 & -1/\mathrm{d}z \times Y_1^2 & \\ 2 & 2+N_{\mathrm{row}}\times N_{\mathrm{col}} & 1/\mathrm{d}z \times Y_1^2 & \\ \vdots & \vdots & & \vdots \end{bmatrix}_{2N\times 3}$$

Additionally, the calculations of $\boldsymbol{By}_1$ and $\boldsymbol{Bz}_1$ are similar as that of $\boldsymbol{Bx}_1$. From the above matrices calculations, it can be found that the dimensions of the matrices $\boldsymbol{Bx}_1$, $\boldsymbol{By}_1$ and $\boldsymbol{Bz}_1$ are all reduced from $2 \times (N \times N) \times (N \times N) \times (N \times 1)$ to $2 \times (2 \times N \times 3) \times (N \times 1) \times (2 \times N \times 3)$ and the magnitude of the calculation amount is reduced to the $1/N^2$ of that of the traditional method. Additionally, this strategy can be also applied to the operations on $\boldsymbol{Bx}_2$, $\boldsymbol{By}_2$ and $\boldsymbol{Bz}_2$.

Then, considering the computations of $\boldsymbol{Bx}_1\boldsymbol{m}_1$, $\boldsymbol{By}_1\boldsymbol{m}_1$, and $\boldsymbol{Bz}_1\boldsymbol{m}_1$ in the cross-gradient constraint.

$$\boldsymbol{Bx}_1\boldsymbol{m}_1 = \boldsymbol{Bx}_1^1\boldsymbol{m}_1 - \boldsymbol{Bx}_1^2\boldsymbol{m}_1$$

$$= \begin{bmatrix} 1 & 1 & -1/\mathrm{d}y \times Z_1^1 \\ 1 & 1+N_{\mathrm{col}} & 1/\mathrm{d}y \times Z_1^1 \\ 2 & 2 & -1/\mathrm{d}y \times Z_1^2 \\ 2 & 2+N_{\mathrm{col}} & 1/\mathrm{d}y \times Z_1^2 \\ \vdots & & \end{bmatrix}_{2N\times 3} \begin{bmatrix} \boldsymbol{m}_1^1 \\ \boldsymbol{m}_1^2 \\ \boldsymbol{m}_1^3 \\ \boldsymbol{m}_1^4 \\ \vdots \end{bmatrix}_{N\times 1} - \begin{bmatrix} 1 & 1 & -1/\mathrm{d}z \times Y_1^1 \\ 1 & 1+N_{\mathrm{row}}\times N_{\mathrm{col}} & 1/\mathrm{d}z \times Y_1^1 \\ 2 & 2 & -1/\mathrm{d}z \times Y_1^2 \\ 2 & 2+N_{\mathrm{row}}\times N_{\mathrm{col}} & 1/\mathrm{d}z \times Y_1^2 \\ \vdots & & \end{bmatrix}_{2N\times 3} \begin{bmatrix} \boldsymbol{m}_1^1 \\ \boldsymbol{m}_1^2 \\ \boldsymbol{m}_1^3 \\ \boldsymbol{m}_1^4 \\ \vdots \end{bmatrix}_{N\times 1}$$

$$= \begin{bmatrix} -1/\mathrm{d}y \times Z_1^1 \times \boldsymbol{m}_1^1 + 1/\mathrm{d}y \times Z_1^1 \times \boldsymbol{m}_1^{1+N_{\mathrm{col}}} \\ -1/\mathrm{d}y \times Z_1^2 \times \boldsymbol{m}_1^2 + 1/\mathrm{d}y \times Z_1^2 \times \boldsymbol{m}_1^{2+N_{\mathrm{col}}} \\ \vdots \end{bmatrix}_{N\times 1} - \begin{bmatrix} -1/\mathrm{d}z \times Y_1^1 \times \boldsymbol{m}_1^1 + 1/\mathrm{d}z \times Y_1^1 \times \boldsymbol{m}_1^{1+N_{\mathrm{row}}\times N_{\mathrm{col}}} \\ -1/\mathrm{d}z \times Y_1^2 \times \boldsymbol{m}_1^2 + 1/\mathrm{d}z \times Y_1^2 \times \boldsymbol{m}_1^{2+N_{\mathrm{row}}\times N_{\mathrm{col}}} \\ \vdots \end{bmatrix}_{N\times 1} = \begin{bmatrix} X_1^{*1} \\ X_1^{*2} \\ \vdots \end{bmatrix}_{N\times 1}$$

Furthermore, the calculations of $\boldsymbol{By}_1\boldsymbol{m}_1$ and $\boldsymbol{Bz}_1\boldsymbol{m}_1$ are similar as $\boldsymbol{Bx}_1\boldsymbol{m}_1$. The dimensions of $\boldsymbol{Bx}_1\boldsymbol{m}_1$, $\boldsymbol{By}_1\boldsymbol{m}_1$ and $\boldsymbol{Bz}_1\boldsymbol{m}_1$ are reduced from $(N\times N)\times(N\times 1)$ to $2\times(2\times N\times 3)\times(N\times 1)$. Obviously, the magnitude of the quantity is reduced to the $1/N$ of that of the original method. Additionally, this strategy also can be applied to the operations on $\boldsymbol{Bx}_2\boldsymbol{m}_2$, $\boldsymbol{By}_2\boldsymbol{m}_2$ and $\boldsymbol{Bz}_2\boldsymbol{m}_2$.

Finally, the $\boldsymbol{Bx}_1^{\mathrm{T}}\boldsymbol{Bx}_1\boldsymbol{m}_1$, $\boldsymbol{By}_1^{\mathrm{T}}\boldsymbol{By}_1\boldsymbol{m}_1$, and $\boldsymbol{Bz}_1^{\mathrm{T}}\boldsymbol{Bz}_1\boldsymbol{m}_1$ are computed using the triple method.

$$\begin{cases} \boldsymbol{Bx}_1^{\mathrm{T}}\boldsymbol{Bx}_1\boldsymbol{m}_1 = \left(\boldsymbol{Bx}_1^{1\mathrm{T}} - \boldsymbol{Bx}_1^{2\mathrm{T}}\right)\boldsymbol{Bx}_1\boldsymbol{m}_1 \\ \boldsymbol{By}_1^{\mathrm{T}}\boldsymbol{By}_1\boldsymbol{m}_1 = \left(\boldsymbol{By}_1^{1\mathrm{T}} - \boldsymbol{By}_1^{2\mathrm{T}}\right)\boldsymbol{By}_1\boldsymbol{m}_1 \\ \boldsymbol{Bz}_1^{\mathrm{T}}\boldsymbol{Bz}_1\boldsymbol{m}_1 = \left(\boldsymbol{Bz}_1^{1\mathrm{T}} - \boldsymbol{Bz}_1^{2\mathrm{T}}\right)\boldsymbol{Bz}_1\boldsymbol{m}_1 \end{cases} \tag{10}$$

In Eq. (10), $\boldsymbol{Bx}_1^{\mathrm{T}}\boldsymbol{Bx}_1\boldsymbol{m}_1$ is calculated by the triple method and the corresponding equations can be expressed as follows.

$$\left(\boldsymbol{Bx}_1^{1\mathrm{T}} - \boldsymbol{Bx}_1^{2\mathrm{T}}\right)\boldsymbol{Bx}_1\boldsymbol{m}_1 = \left\{ \begin{bmatrix} 1 & 1 & -1/\mathrm{d}y \times Z_1^1 \\ 1 & 1+N_{\mathrm{col}} & 1/\mathrm{d}y \times Z_1^1 \\ 2 & 2 & -1/\mathrm{d}y \times Z_1^2 \\ 2 & 2+N_{\mathrm{col}} & 1/\mathrm{d}y \times Z_1^2 \\ \vdots & & \end{bmatrix}_{2N\times 3}^{\mathrm{T}} - \begin{bmatrix} 1 & 1 & -1/\mathrm{d}z \times Y_1^1 \\ 1 & 1+N_{\mathrm{row}}\times N_{\mathrm{col}} & 1/\mathrm{d}z \times Y_1^1 \\ 2 & 2 & -1/\mathrm{d}z \times Y_1^2 \\ 2 & 2+N_{\mathrm{row}}\times N_{\mathrm{col}} & 1/\mathrm{d}z \times Y_1^2 \\ \vdots & & \end{bmatrix}_{2N\times 3}^{\mathrm{T}} \right\} \begin{bmatrix} X_1^{*1} \\ X_1^{*2} \\ \vdots \end{bmatrix}_{N\times 1}$$

$$= \left\{ \begin{bmatrix} a_{11} & b_{11} & c_{11} \\ a_{12} & b_{12} & c_{12} \\ \vdots & & \\ a_{1i} & b_{1i} & c_{1i} \\ \vdots & & \end{bmatrix}_{2N(i=1,2\ldots 2N)}^{\mathrm{T}} - \begin{bmatrix} a_{21} & b_{21} & c_{21} \\ a_{22} & b_{22} & c_{22} \\ \vdots & & \\ a_{2k} & b_{2k} & c_{2k} \\ \vdots & & \end{bmatrix}_{2N(k=1,2\ldots 2N)}^{\mathrm{T}} \right\} \begin{bmatrix} X_1^{*1} \\ X_1^{*2} \\ \vdots \end{bmatrix}_{N\times 1(j=1,2\ldots N)}$$

$$= \left[\sum_{i=1,b_{1i}=j}^{2N} c_{1i} X_1^{*a_{1i}} - \sum_{k=1,b_{2k}=j}^{2N} c_{2k} X_{b1}^{*a_{2k}} \right]_{N\times 1(j=1,2\ldots N)}$$

The dimensions of the $\boldsymbol{Bx}_1^{\mathrm{T}}\boldsymbol{Bx}_1\boldsymbol{m}_1$, $\boldsymbol{By}_1^{\mathrm{T}}\boldsymbol{By}_1\boldsymbol{m}_1$ and $\boldsymbol{Bz}_1^{\mathrm{T}}\boldsymbol{Bz}_1\boldsymbol{m}_1$ during the calculations are reduced from $(N\times N)\times(N\times N)\times(N\times 1)$ to $(2\times N\times 3)\times(2\times N\times 3)\times(N\times 1)$, suggesting that the magnitude of the calculation amount is reduced to the $1/N^2$ of that of the original method. In addition, this strategy also applies to compute $\boldsymbol{Bx}_2\boldsymbol{m}_2$, $\boldsymbol{By}_2\boldsymbol{m}_2$ and $\boldsymbol{Bz}_2\boldsymbol{m}_2$. In this paper, the model weighting and re-weighting strategies are also adopted to improve the accuracy and speed up the convergence efficiency of the fast cross-gradient joint inversion.

3. Results and validation

Synthetic data and field data are adopted to verify the validity and applicability of the developed method in this paper. All inversion calculations are performed on an Intel(R)-Xeon(R)-CPU-E5-2600-V4 2.10-GHz machine with 123 GB RAM.

3.1. Synthetic model test

The synthetic model data is adopted to certificate the original cross-gradient constraint versus the fast cross-gradient constraint. Fig. 2a and b presents a 3-D view of the synthetic model. The density model includes 2 hexahedrons with uniform density, while the magnetization model contains a uniform layered model.

The cross-gradient values of the above synthetic models are calculated by the original cross-gradient method and the fast cross-gradient method, respectively. Fig. 3a and b illustrate the slices of cross-gradient values calculated by the original method. Fig. 3c and d represent the slices of the cross-gradient values calculated by the fast method. It can be found that the cross-gradient values calculated by the 2 methods are consistent with each other, suggesting the correctness of the fast cross-gradient constraint. Obviously, both calculation methods can obtain the boundaries of the same structure of the 2 physical property models, suggesting that the 2 cross-gradient constraints have the same structural coupling capability.

The maximum memory consumptions among different computational methods are listed in Table 1 for different meshes to certificate the efficiency of the proposed method. In the inversion process, the Jacobian matrix is calculated during each iteration, rather than storing the Jacobian matrix at the beginning of the inversion. From Table 1, the memory requirements can be effectively reduced by using the fast cross-gradient joint inversion method. The more grid cells are divided, the higher the reduction rate of the computing memory required.

A synthetic model data is adopted to certificate the applicability of the developed method in this paper. Fig. 4a and b presents a 3-D view of the synthetic model. The data on the surface are generated on a grid with $21 \times 21 = 441$ points and a grid spacing of 100 m. The gravity and magnetic data computed from the synthetic model are presented in Fig. 4c and d, respectively. To perform the inversion, the subsurface volume is discretized into $20 \times 20 \times 10$ prisms of sizes 100 m in each dimension. The bound constraints $0 = m_1^- \leq \boldsymbol{m}_1 \leq m_1^+ = 1.0$ g/cc, and $0 = m_2^- \leq \boldsymbol{m}_2 \leq m_2^+ = 1.0$ A/m, are imposed on all inversions.

The number of iterations is set to 100, the initial density model and the reference density model are set to 0.01 g/cc and 0 g/cc,

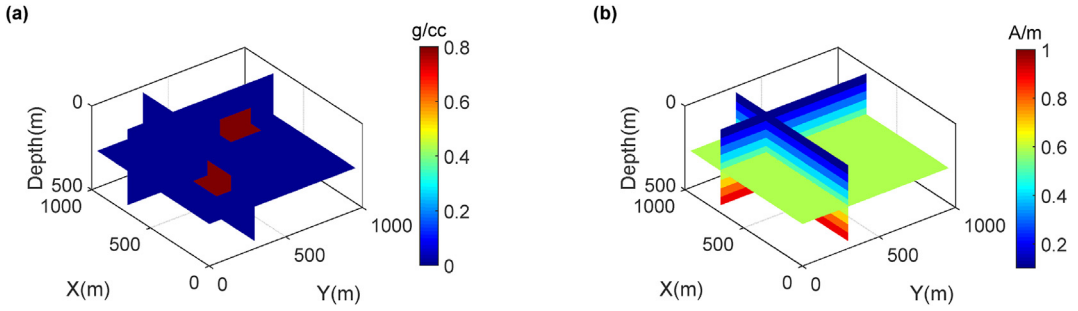

Fig. 2. Schematic representation of the density and the magnetization models with a non-zero cross gradient. (a) Represents density model and (b) represents magnetization model.

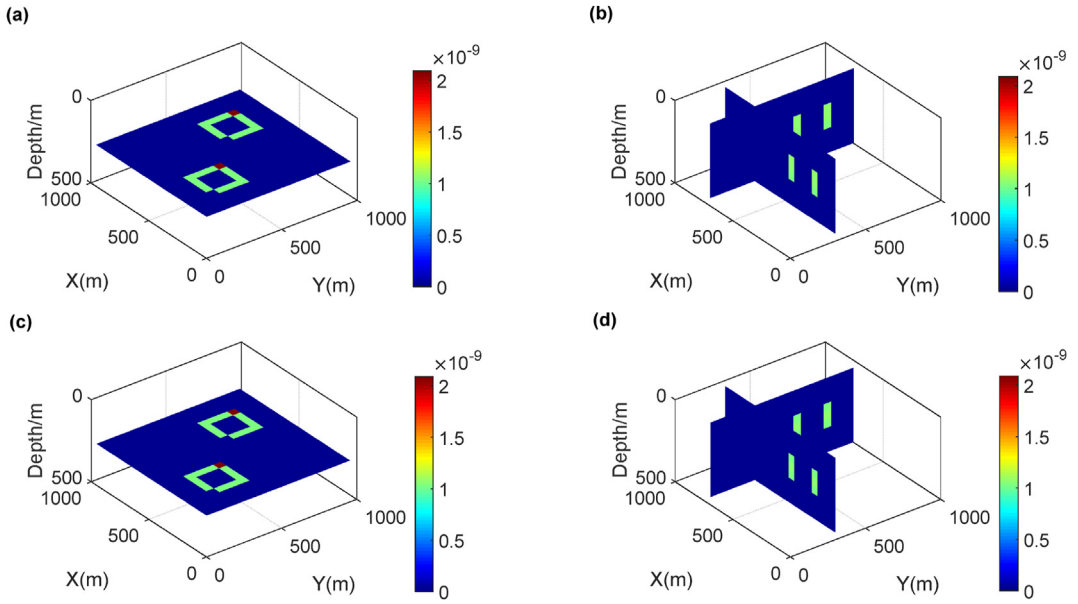

Fig. 3. The slices of the cross-gradient values obtained from the original method at $z = 250$ m (a), at $x = 700$ m and $y = 300$ m (b). The slice of the cross-gradient values obtained from the fast method at $z = 250$ m (c), at $x = 700$ m and $y = 300$ m (d).

Table 1
Maximum memory cost in the joint inversion of synthetic data.

Meshing Memory Cost	20 × 20 × 10	30 × 30 × 15	40 × 40 × 20
Cross-gradient joint Inversion	0.871 GB	5.207 GB	102.323 GB
Fast cross-gradient joint inversion	0.454 GB	0.457 GB	0.468 GB

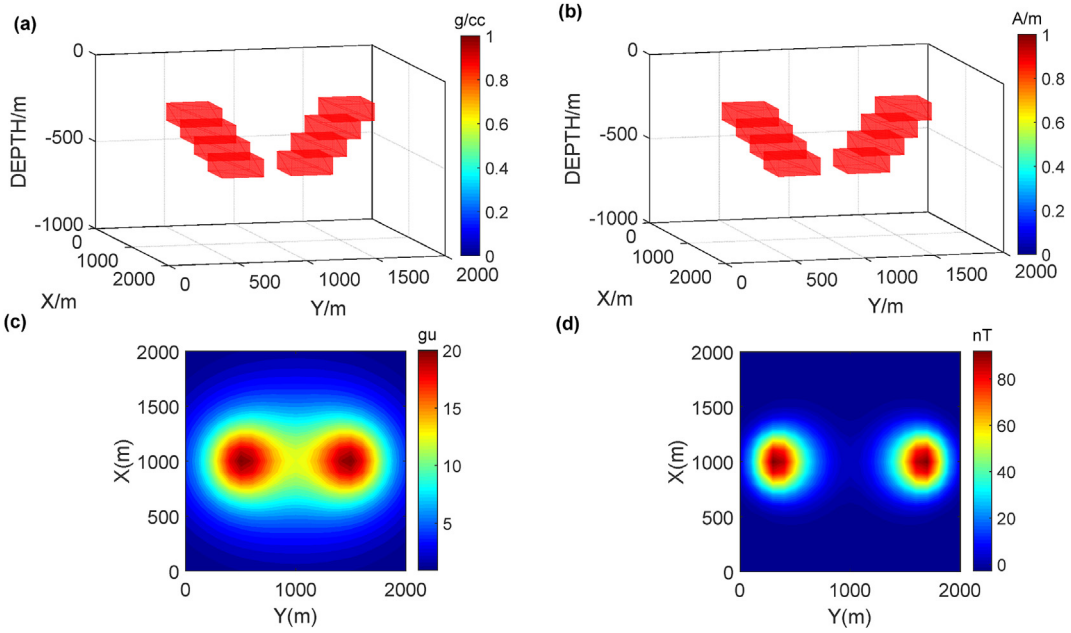

Fig. 4. Spatial location of the synthetic models for density model (a) and magnetization model (b). (c) The contour map of forward gravity anomaly of the density model. (d) The contour map of the forward magnetic anomaly of the magnetization model.

respectively, and the initial magnetization model and the reference magnetization model are set to 0.01 A/m and 0 A/m, respectively. The parameters of the regularization method are $\tau_1 = 0.01$ and $\varepsilon = 0.001$. Then, separate inversions of the gravity and magnetic data are performed. Fig. 5a and b represent the slices of the recovered density model at $x = 1000$ m and $z = 400$ m, respectively. Fig. 5c and d illustrate the slices of the recovered magnetization model at $x = 1000$ m and $z = 400$ m, respectively. From Figs. 4 and 5, the recovered density and magnetization models can delineate the distribution of geology anomalous bodies.

Then, the weighting parameters of the cross-gradient constraints are set to 1.0^{10}, the rest parameters are the same as those for separate inversions, and the original cross-gradient joint inversion of gravity and magnetic data are performed. Fig. 6a and b illustrate the slices of the recovered density model at $x = 1000$ m and $z = 400$ m. Fig. 6c and d represent the slices of the recovered magnetization model at $x = 1000$ m and $z = 400$ m. From Figs. 5 and 6, the recovered density model and magnetization model of the joint inversion are closer to the values of the actual model and the structural consistency of joint inversion results is also higher. Additionally, the time for original cross-gradient joint inversion is 28 min.

Then, the parameters are consistent with those of the original joint inversion, and the fast inversion is conducted. Fig. 7a and b represent the slices of the recovered density model at $x = 1000$ m and $z = 400$ m. Fig. 7c and d represent the slices recovered magnetization model at $x = 1000$ m and $z = 400$ m. From Figs. 6 and 7, it can be found that the recovered models obtained from the 2 methods are very close, which can be considered that both methods can play the role of structural coupling constraints. The computation time of the fast cross-gradient joint inversion is 7 min, which is 1/4 of the computation time of the original cross-gradient joint inversion and indicates that the computing efficiency is greatly improved. Furthermore, the reconstructed accuracy of the fast cross-gradient joint inversion compared to the recovered accuracy of the separate inversions is also significantly modified.

Fig. 8 represent the cross-gradient values calculated from the recovered models. Fig. 8a–c illustrate the vertical slices of the cross-gradient values at $x = 1000$ m calculated from the recovered results of the separate inversions, the original cross-gradient joint inversion and the fast cross-gradient joint inversion, respectively. Additionally, Fig. 8d–f illustrate the horizontal slices of the cross-gradient values at $z = 400$ m calculated from the recovered results of separate inversion, the cross-gradient joint inversion and the fast cross-gradient joint inversion, respectively. It can be found that the boundaries of anomalous geology bodies can be recognized from the cross-gradient values of the joint inversion results. Simultaneously, the cross-gradient values of the fast inversion are very similar to the cross-gradient values of the original inversion, indicating that the fast inversion method also covers the ability of the structural coupling constraint. In addition, the cross-gradient values of the 2 joint inversions are lower than that of the separate inversions, and the spatial distribution of the former is also more reasonably distributed around the geology anomalous bodies.

Furthermore, the subsurface volume is discretized into 30 × 30 × 15 prisms to verify the efficiency of the developed method in this paper. The number of iterations is adjusted to 40, the weighting parameters of the cross-gradient constraint for gravity and magnetic data are both set to 1.0^9, and the remaining parameters are consistent with those parameters of the previous joint

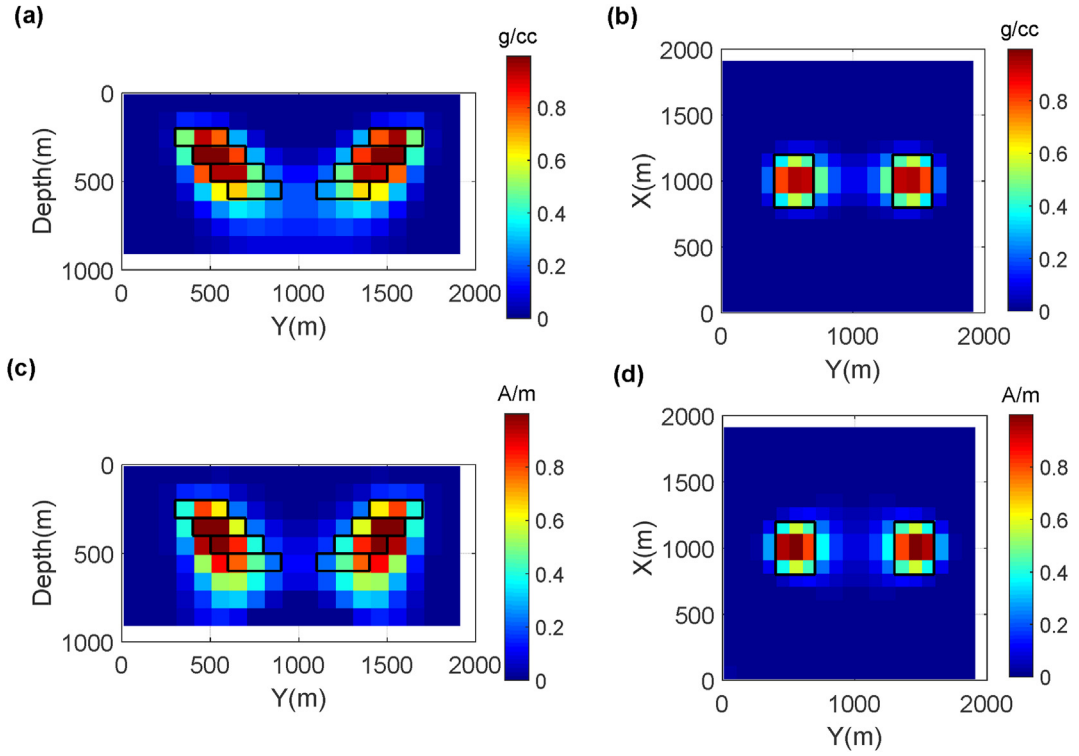

Fig. 5. The separate inversions of synthetic data. (a) and (b) are the slices of the recovered density model at $x = 1000$ m and $z = 400$ m, respectively. (c) and (d) are the slices of the recovered magnetization model at $x = 1000$ m and $z = 400$ m, respectively. The black boxes in Fig. 5 are the locations of the actual models.

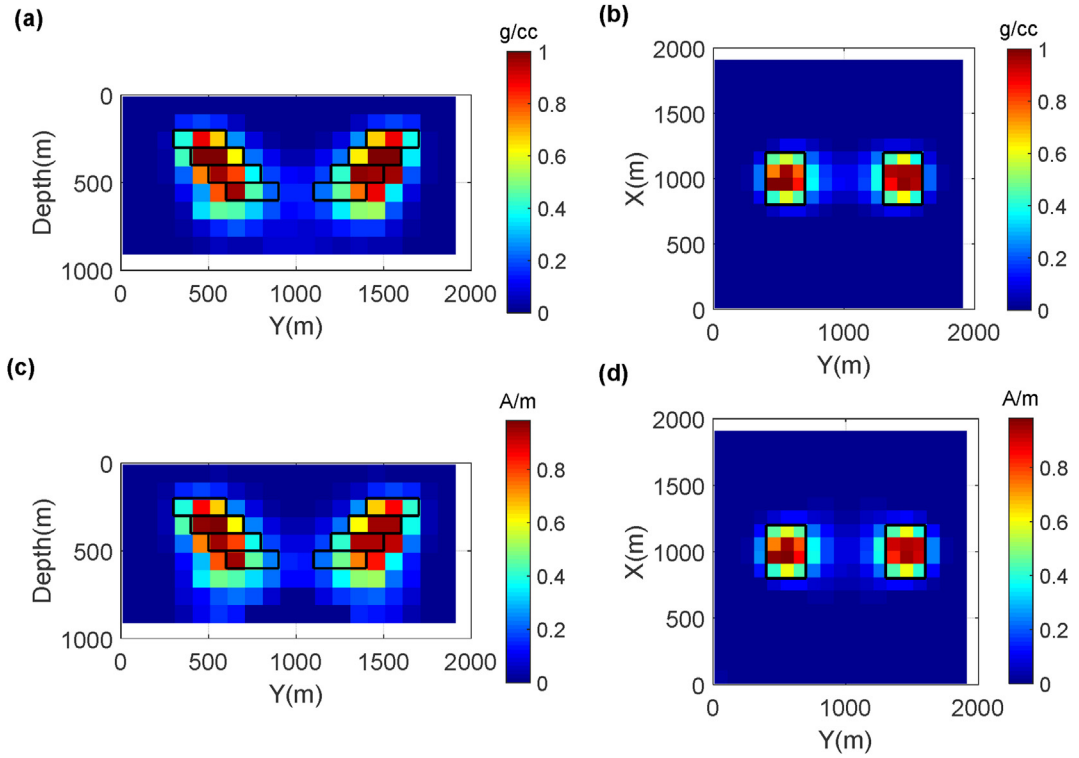

Fig. 6. The original cross-gradient joint inversion of synthetic data. (a) and (b) represent the slices of the recovered density model at $x = 1000$ m and $z = 400$ m, respectively. (c) and (d) represent the slices of the recovered magnetization model at $x = 1000$ m and $z = 400$ m, respectively. The black boxes represent the locations of the actual models.

inversion. Then, the original cross-gradient joint inversion is conducted. Fig. 9a–d illustrate the slices of the reconstructed models, respectively. Additionally, the computation time of the original joint inversion is 137 min.

Then, the weighting parameters of the fast cross-gradient constraint are set to 5.0^8, the remaining parameters are consistent with those of the previous original joint inversion, and the fast cross-gradient joint inversion based on the refinement meshing is

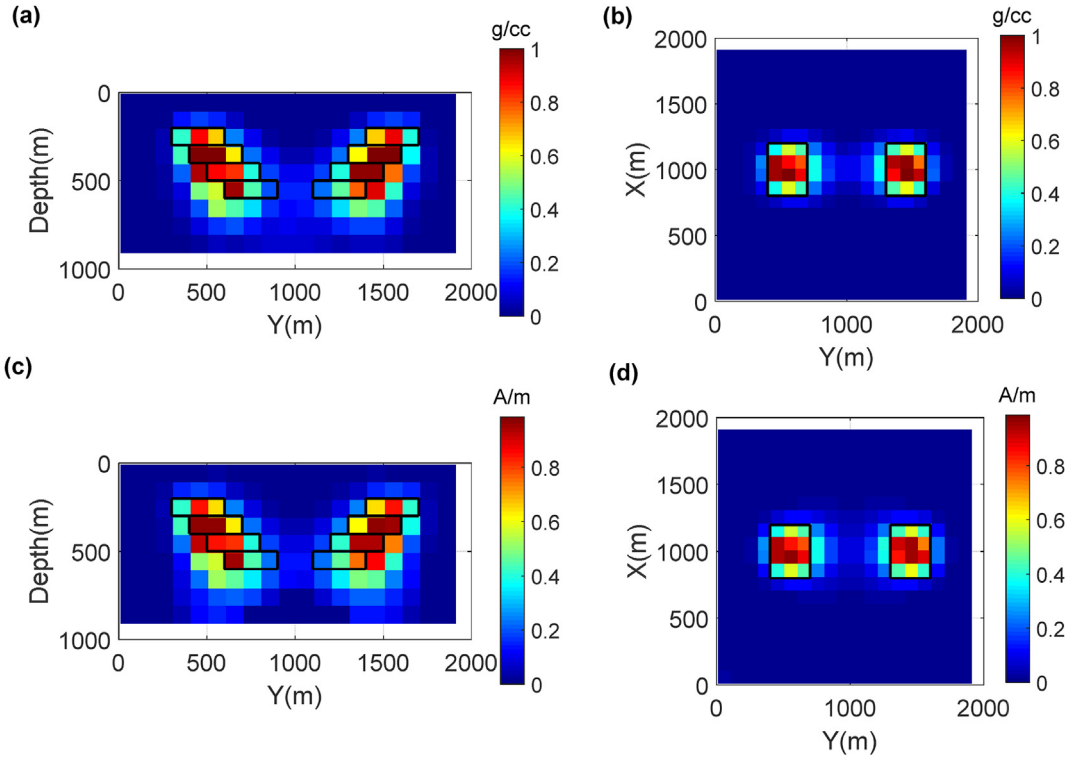

Fig. 7. The fast cross-gradient joint inversion of synthetic data. (a) and (b) represent the slices of the recovered density model at $x = 1000$ m and $z = 400$ m, respectively. (c) and (d) represent the slices of the recovered magnetization model at $x = 1000$ m and $z = 400$ m, respectively. The black boxes represent the locations of the synthetic models.

conducted for the synthetic data. Fig. 10a–d represent the slices of the recovered physical property models, respectively. The computing time of the fast inversion is reduced to 14 min, which is 1/10 times the computing time of the original joint inversion. Additionally, from Figs. 9 and 10, the recovered results of the 2 joint inversions are very close, which once again certificates that the fast method covers the same structural coupling ability as the original method.

The cross-gradient values calculated from the recovered models are displayed in Fig. 11. Fig. 11a and c represent the slices of the cross-gradient values derived from the recovered results of the original cross-gradient joint inversion, respectively. Fig. 11b and d represent the slices of the cross-gradient values calculated from the reconstructed results of the fast cross-gradient joint inversion, respectively. It also can be found that the cross-gradient values of

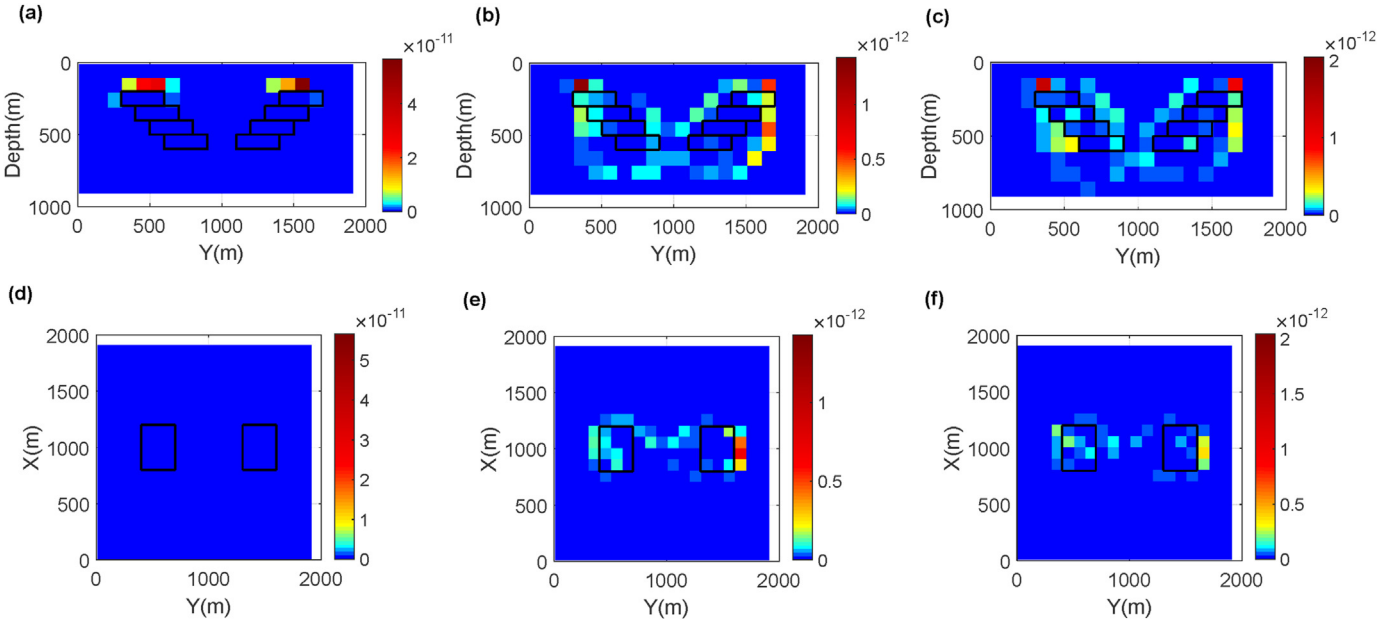

Fig. 8. The vertical slice (a) and horizontal slice (d) of the cross-gradient values from the separate inversions, the vertical slice (b) and horizontal slice (e) of the cross-gradient values from the original cross-gradient joint inversion, and the vertical slice (c) and horizontal slice (f) of cross-gradient values from the fast cross-gradient joint inversion. The black box represents the location of the actual models.

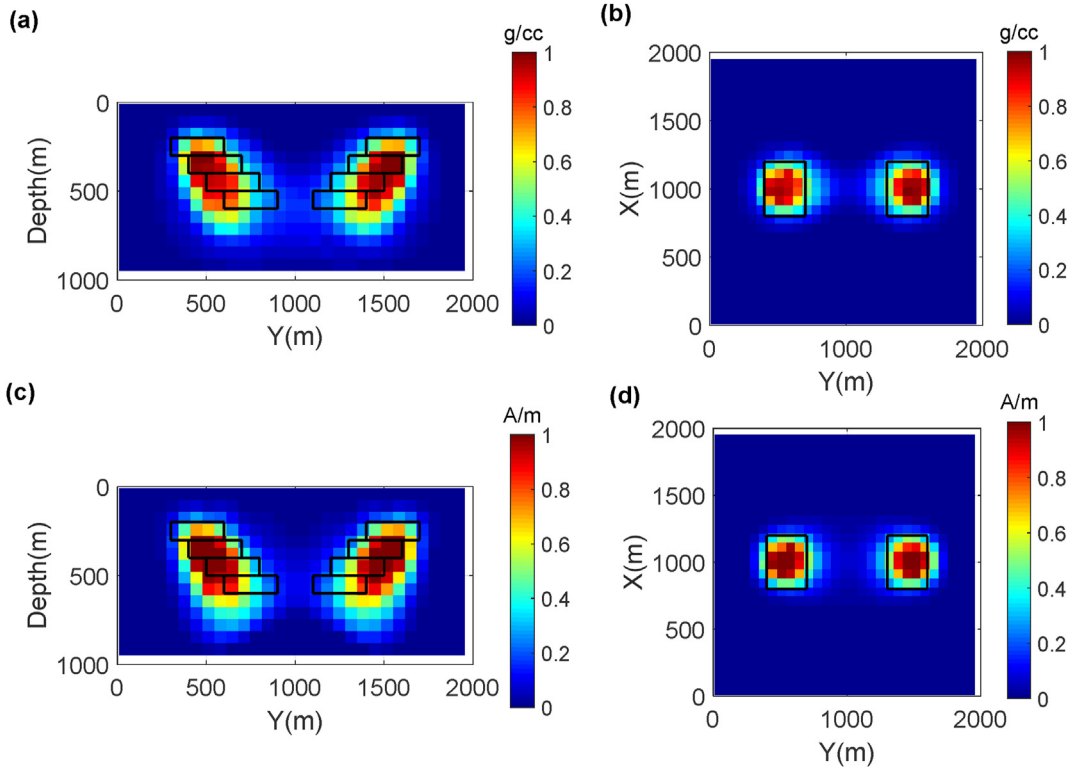

Fig. 9. The original cross-gradient joint inversion of synthetic data. (a) and (b) represent the slices of the recovered density model at $x = 1000$ m and $z = 400$ m, respectively. (c) and (d) represent the slices of the recovered magnetization model at $x = 1000$ m and $z = 400$ m, respectively. The black boxes are the locations of the actual models.

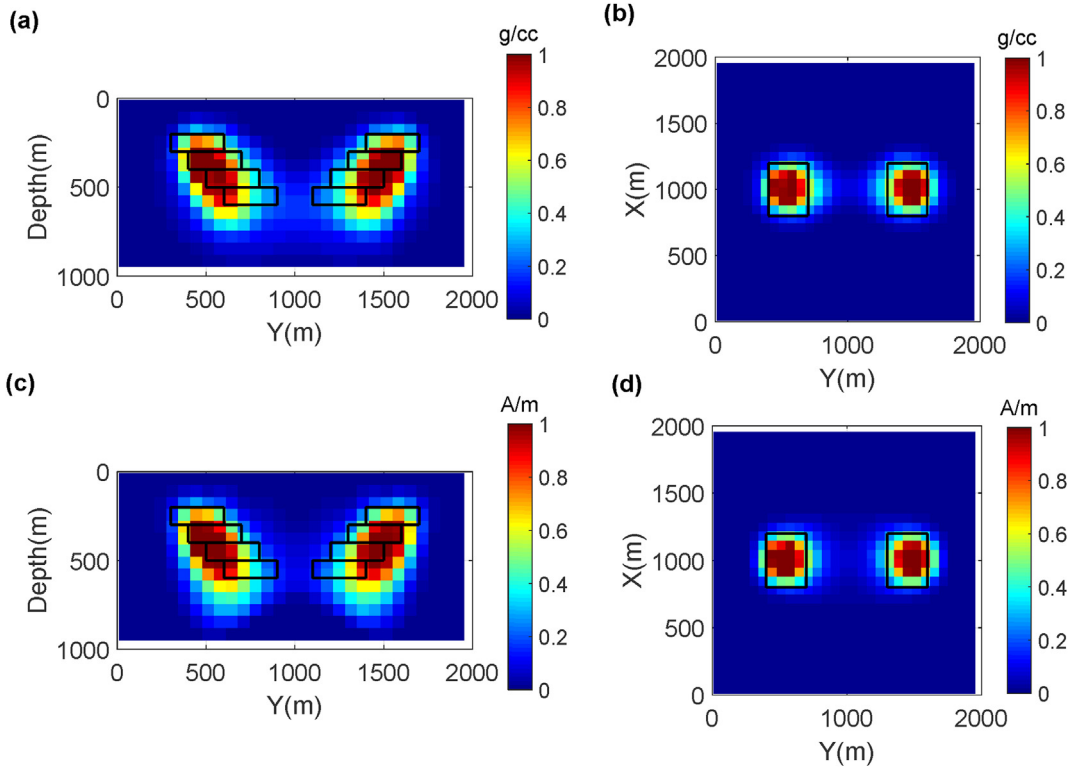

Fig. 10. The fast cross-gradient joint inversion of synthetic data. (a) and (b) represent the slices of the recovered density model at $x = 1000$ m and $z = 400$ m, respectively. (c) and (d) represent the slices of the recovered magnetization model at $x = 1000$ m and $z = 400$ m, respectively. The black boxes are the locations of the actual models.

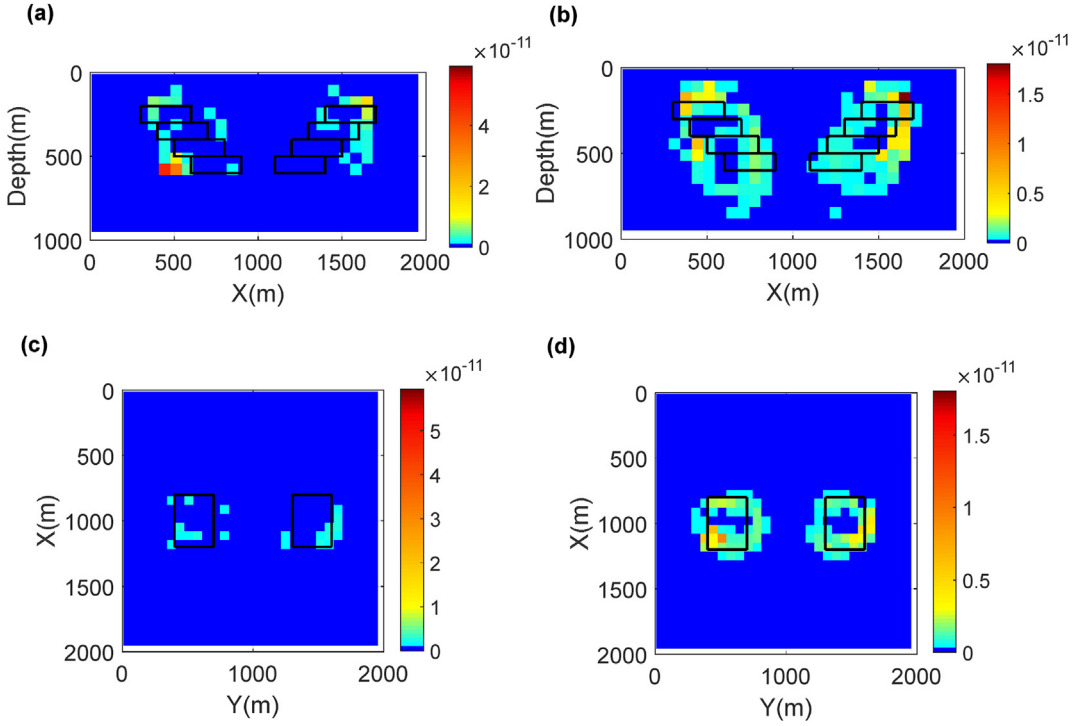

Fig. 11. The vertical slice (a) and horizontal slice (c) of cross-gradient values from the original cross-gradient joint inversion, and the vertical slice (b) and horizontal slice (d) of cross-gradient values from the fast cross-gradient joint inversion. The black box represents the location of the actual models.

the fast cross-gradient joint inversion are very similar to that of the original cross-gradient joint inversion, indicating that the fast cross-gradient joint inversion method also has the ability of the structural consistency constraint of the original cross-gradient joint inversion method.

3.2. Application to the field data

The joint inversion is applied to interpreting of field data in the Baoshan lead-zinc-silver polymetallic mining area in Hunan Province, China. After removing the regional gravity anomalies from the observed gravity anomalies, the residual gravity anomalies (Fig. 12a) are acquired. Simultaneously, the regional magnetic field is subtracted from the observed magnetic anomaly data (Fig. 12b). The observed gravity and magnetic data is a regular grid of 41 × 31, with a total of 1271 equidistant data points. The subsurface volume is discretized into 30 × 20 × 12 prisms. From prior petrophysical information obtained from the borehole data in the mining area, the bound constraints $-1.0 = \mathrm{m}_1^- \leq \boldsymbol{m}_1 \leq \mathrm{m}_1^+ = 3.0$ g/cc, and $-1.0 = \mathrm{m}_2^- \leq \boldsymbol{m}_2 \leq \mathrm{m}_2^+ = 3.0$ A/m, are imposed.

Firstly, the initial density and initial magnetization models are homogeneous half-space models of 0.1 g/cc and 0.1 A/m, respectively. The number of iterations is set to 70, the parameters of the regularization method are set to $\tau_1 = 0.9$, $\varepsilon = 0.1$, and the separate inversions of gravity and magnetic data are conducted, respectively. Fig. 13a–c represent the slices of the reconstructed density model at $z = 250$ m, $z = 450$ m and $z = 650$ m, respectively. Fig. 13d–f represent the slices of the recovered magnetization model at $z = 250$ m, $z = 450$ m and $z = 650$ m, respectively. Obviously, from Fig. 13, the reconstructed models of separate inversions can present the spatial distribution of underground geological bodies.

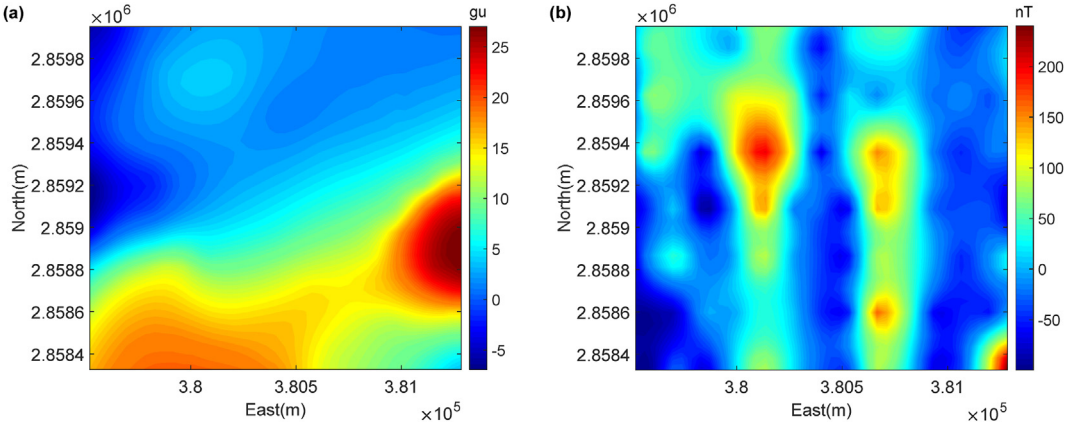

Fig. 12. Observed data in the Baoshan mining area. (a) Residual gravity anomaly and (b) magnetic anomaly.

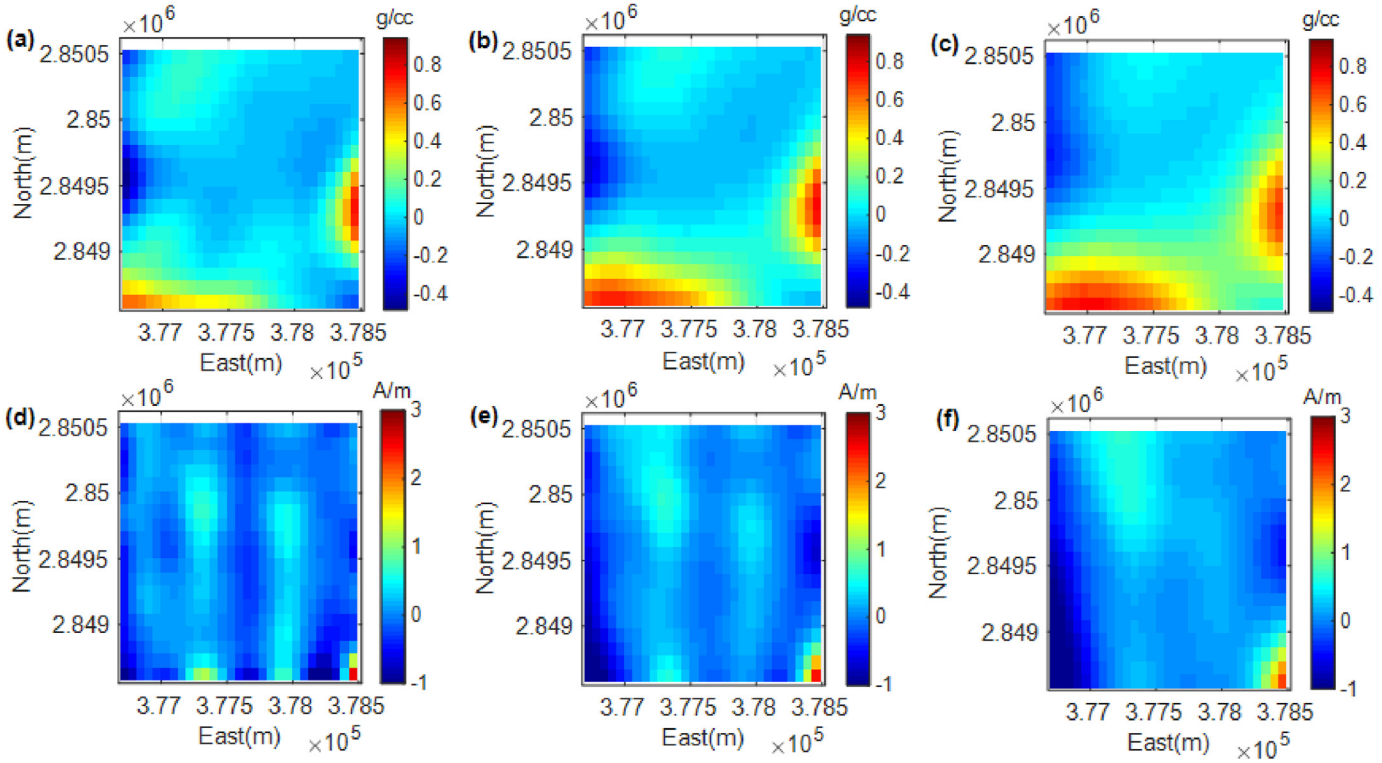

Fig. 13. The result of the separate inversions of gravity and magnetic data. The slices of the recovered density model at $z = 250$ m (a), $z = 450$ m (b) and $z = 650$ m (c). The slices of the recovered magnetization model at $z = 250$ m (d), $z = 450$ m (e) and $z = 650$ m (f).

Then, the weighting parameters of the cross-gradient constraints are to 5.0^{11}, the rest parameters are the same as those of the separate inversions, and the original cross-gradient joint inversion for the gravity and magnetic data are conducted. Fig. 14a–c represent the slices of the recovered density model at $z = 250$ m, $z = 450$ m and $z = 650$ m. Fig. 14d–f represent the slices of the

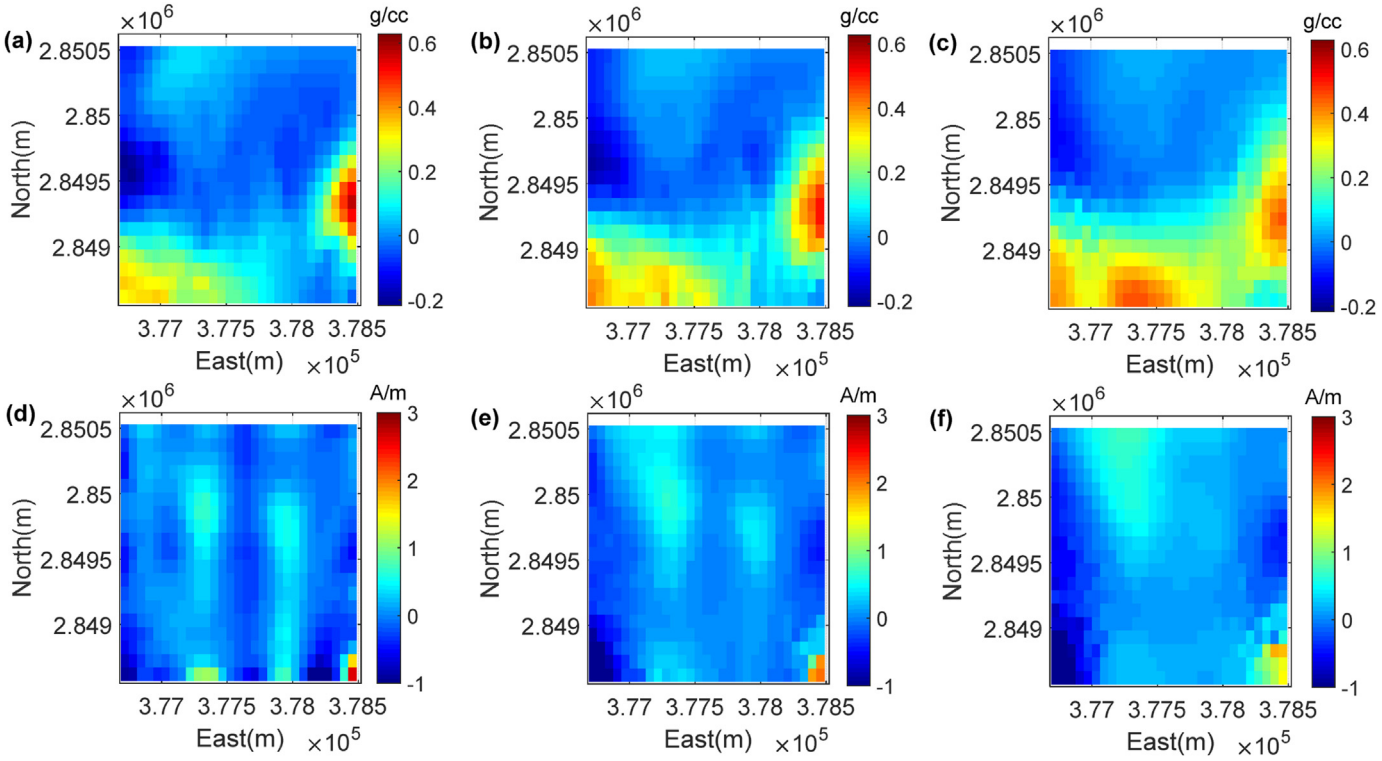

Fig. 14. The result of the original cross-gradient joint inversion of gravity and magnetic data. The slices of the recovered density model at $z = 250$ m (a), $z = 450$ m (b) and $z = 650$ m (c). The slices of the recovered magnetization model at $z = 250$ m (d), $z = 450$ m (e) and $z = 650$ m (f).

reconstructed magnetization model at $z = 250$ m, $z = 450$ m and $z = 650$ m. The computing time of the original cross-gradient joint inversion is 71 min. From Figs. 13 and 14, the reconstructed models of the original joint inversion differ from those of the separate inversions, especially the spatial distributions of density and magnetization models present certain structural consistency. Additionally, the recovered results of the joint inversion are more detailed in the description of spatial distributions, which presents that the recovered models of the gravity and magnetic data have a good mutual constraint effect and reduce the diversity of solutions.

Furthermore, the weighting parameters are consistent with those of the previous original joint inversion for field data, and then the fast cross-gradient joint inversion is conducted. Fig. 15a–c represent the slices of the reconstructed density model at $z = 250$ m, $z = 450$ m and $z = 650$ m, respectively. Fig. 15d–f represent the slices of the reconstructed magnetization model at $z = 250$ m, $z = 450$ m and $z = 650$ m, respectively. Obviously, from Figs. 14 and 15, it can be found that the 2 reconstructed models are very close, both models can accurately delineate the distribution of anomalous geology bodies, and the density model obtains more similar underground structure distribution through the contribution of the structural constraints of the recovered magnetization model. In addition, the computing time of the fast cross-gradient joint inversion is 12 min, which is only 0.17 times the computing time of the original cross-gradient joint inversion. Simultaneously, the maximum memory consumptions for field data inversions among different methods are listed in Table 2 and the memory requirements can be effectively reduced by using the fast cross-gradient joint inversion method. Therefore, this improved calculation efficiency can once again prove that the fast method's computation efficiency is much higher than that of the original method.

Fig. 16 represents the cross-gradient values calculated from the recovered models. Fig. 16a and d illustrate the slices of the cross-gradient values derived from the recovered results of the separate inversions, respectively. Fig. 16b and e represent the slices of the cross-gradient value calculated from the recovered results of the original cross-gradient joint inversion, respectively. Fig. 16c and f represent the slices of the cross-gradient value calculated from the recovered results of the fast cross-gradient joint inversion, respectively. Apparently, it can be found that the cross-gradient values of the 2 joint inversion results are much smaller than that of the separate inversion results, which implies that the reconstructed density model and magnetization model from the 2 cross-gradient joint inversions cover a higher degree of structural coupling.

Table 2
Maximum memory cost in the joint inversion of field data.

Meshing Memory Cost	$30 \times 20 \times 12$
Cross-gradient joint Inversion	1.90 GB
Fast cross-gradient joint inversion	0.477 GB

4. Conclusions

In this paper, a fast cross-gradient joint inversion method for gravity and magnetic data is developed based on the storage and operation strategies of the triple sparse matrices, and then the joint inversion is conducted in the parametric domain. The triple method is adopted to optimize the storage and computation of the sparse matrices' operations involving physical property models' gradients, which need not operate on all elements of those sparse matrices, and only needs to conduct on non-zero elements. The developed method in this paper was validated by synthetic data, and the reconstructed results present that the proposed fast cross-gradient joint inversion method can effectively achieve structural consistency coupling and

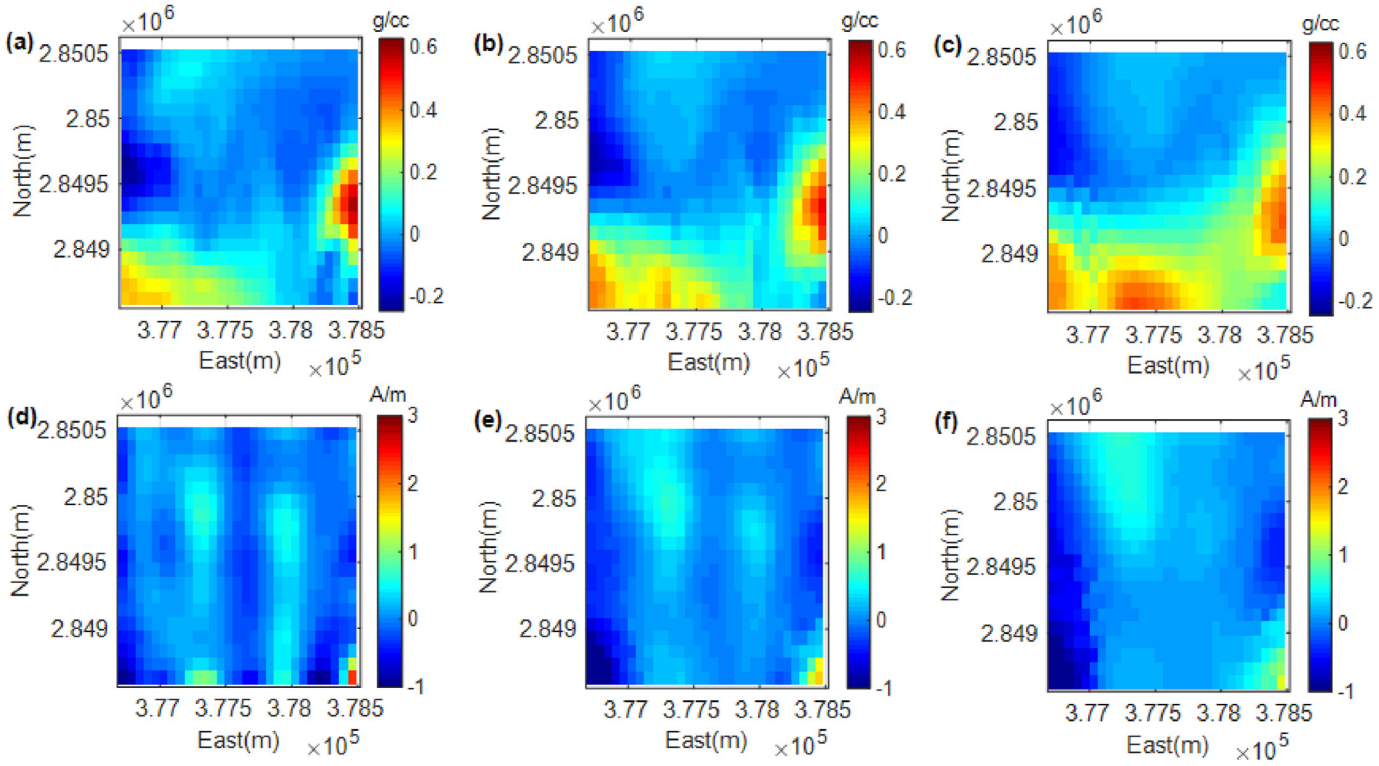

Fig. 15. The result of the fast cross-gradient joint inversion of gravity and magnetic data. The slices of the recovered density model at $z = 250$ m (a), $z = 450$ m (b) and $z = 650$ m (c). The slices of the recovered magnetization model at $z = 250$ m (d), $z = 450$ m (e) and $z = 650$ m (f).

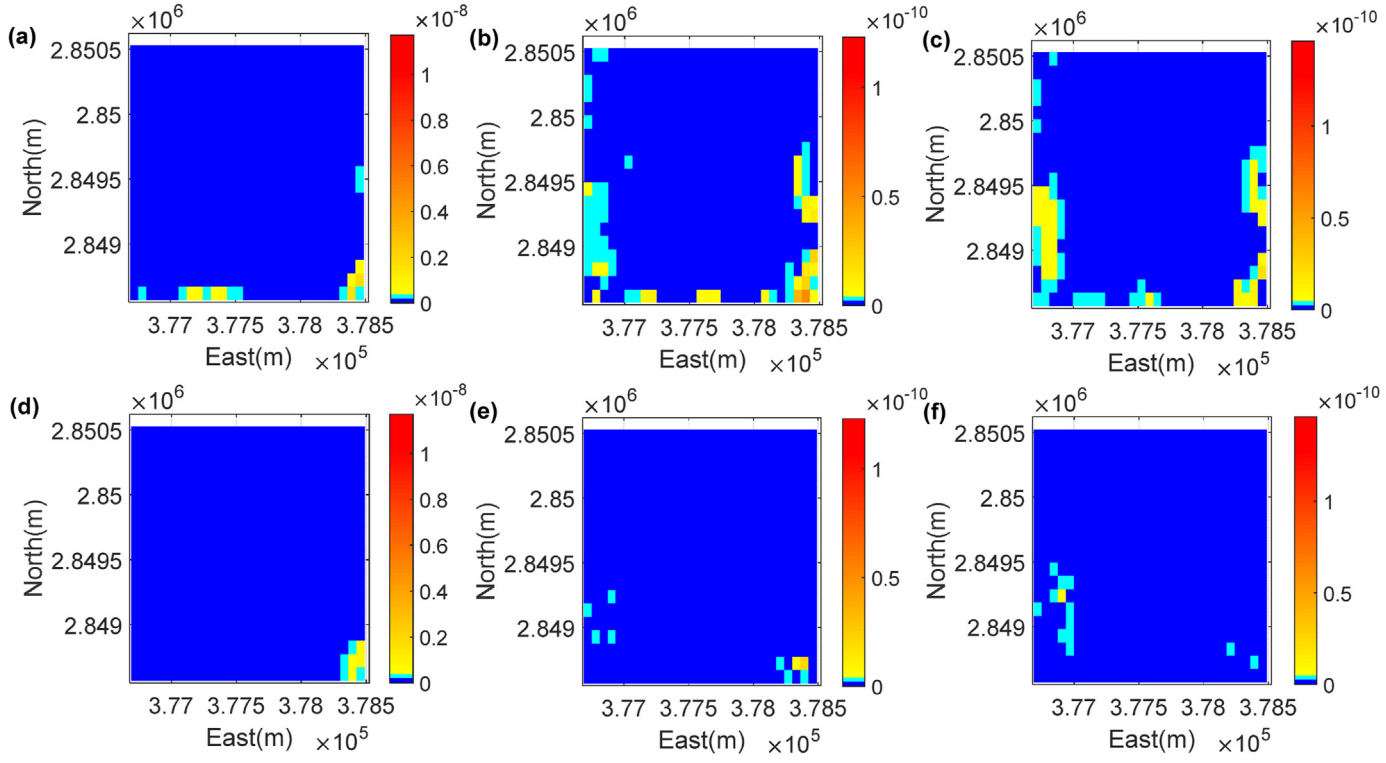

Fig. 16. The cross-gradient values from the individual inversion at (a) $z = 250$ m and (d) $z = 450$ m. The cross-gradient values from the original inversion results at (b) $z = 250$ m and (e) $z = 450$ m. The cross-gradient values from the fast inversion results at (c) $z = 250$ m and (f) $z = 450$ m.

improve the accuracy of recovered models when compared with the separate inversions, and effectively improve the computational efficiency of the original cross-gradient joint inversion. In addition, the relevant calculations' storage involving the gradients' matrices of the physical models is compressed to at least a fraction of the number of meshing units in the memory required by the original cross-gradient joint method. When the number of meshing units increases, the memory compression ratio increases. Furthermore, the inversions of the field data verified the proposed method's effectiveness and stability, and proved that the algorithm developed in this paper provided an effective technical method for the detection of the internal structure.

Author contributions

Sheng Liu carried out the analyses, interpreted the results and drafted the manuscript. Shuanggen Jin and Xiangyun Wan guided the study and gave useful advice about the results. Songbai Xuan, Bin Jia, Quan Lou, Binbin Qin, Rongfu Peng and Dali Sun took part in the design of the study. All authors read and approved the final manuscript.

Availability of data and materials

Field data adopted in this paper are available on request from Dr. Sheng Liu.

Declaration of competing interest

Authors have no conflicts of interest to declare.

Acknowledgements

We would like to thank ones who made practical field data in a mining area of Hunan province. Thank anonymous reviewers for their suggestions. This work was supported by the National Key Research and Development Program (Grant No. 2021YFA0716100), the National Key Research and Development Program of China Project (Grant No. 2018YFC0603502) and Henan Youth Science Fund Program (Grant No. 212300410105).

References

[1] N. Linde, A. Tryggvason, J.E. Peterson, et al., Joint inversion of crosshole radar and seismic traveltimes acquired at the south oyster bacterial transport site, Geophysics 73 (4) (2008) G29–G37.
[2] E. Fregoso, L.A. Gallardo, Cross-gradients joint 3D inversion with applications to gravity and magnetic data, Geophysics 74 (4) (2009) L31–L42.
[3] M. Moorkamp, B. Heincke, M. Jegen, A framework for 3D joint inversion of MT, gravity and seismic refraction data, Geophys J Int 184 (1) (2011a) 477–493.
[4] M. Moorkamp, A.W. Roberts, M. Jegen, et al., Verification of velocity-resistivity relationships derived from structural joint inversion with borehole data, Geophys Res Lett 40 (14) (2013) 3596–3601.
[5] G.H.F. Gardner, L.W. Gardner, A.R. Gregory, Formation velocity and density-the diagnostic basics for stratigraphic traps, Geophysics 39 (6) (1974) 770–780.
[6] M. Sun, S.G. Jin, Multiparameter elastic full waveform inversion of ocean bottom seismic four-component data based on a modified acoustic-elastic coupled equation, Rem Sens 12 (17) (2020) 2816.
[7] J. Sun, Y. Li, Multidomain petrophysically constrained inversion and geology differentiation using guided fuzzy c-means clustering, Geophysics 80 (4) (2015) ID1–ID18.
[8] J. Sun, Y. Li, Joint inversion of multiple geophysical data using guided fuzzy c-means clustering, Geophysics 81 (3) (2016) ID37–ID57.
[9] R. Tenzer, W. Chen, S.G. Jin, Effect of the upper mantle density structure on the Moho geometry, Pure Appl Geophys 172 (6) (2015) 1563–1583.
[10] B. Zhang, S.G. Jin, C. Liu, Z. Guo, X. Liu, Prediction of shear wave velocity based on a statistical rock-physics model and Bayesian theory, J Petrol Sci Eng 195 (2020), 107710.

[11] B. Heincke, M. Jegen, R. Hobbs, Joint inversion of MT, gravity and seismic data applied to sub-basalt imaging, SEG Technical Program Expanded Abstracts, 2006.
[12] D. Colombo, M.D. Stefano, Geophysical modeling via simultaneous joint inversion of seismic, gravity, and electromagnetic data: application to pre-stack depth imaging, Lead Edge 26 (3) (2007) 326–331.
[13] L.A. Gallardo, M.A. Meju, Characterization of heterogeneous near-surface materials by joint 2D inversion of dc resistivity and seismic data, Geophys Res Lett 30 (13) (2003).
[14] L.A. Gallardo, M.A. Meju, Joint two-dimensional DC resistivity and seismic traveltime inversion with cross-gradients constraints, J Geophys Res 109 (B3) (2004) 3311–3315.
[15] L.A. Gallardo, Multiple cross-gradient joint inversion for geospectral imaging, Geophys Res Lett 34 (19) (2007), L19301.
[16] L.A. Gallardo, S.L. Fontes, M.A. Meju, M.P. Buonora, P.P. De Lugao, Robust geophysical integration through structure-coupled joint inversion and multispectral fusion of seismic reflection, magnetotelluric, magnetic, and gravity images: example from Santos Basin, offshore Brazil, Geophysics. 77 (2012) B237–B251.
[17] T.L. Li, R.Z. Zhang, Y.C. Pak, et al., Multiple joint inversion of geophysical data with sub-region cross-gradient constraints, Chin J Geophys 59 (8) (2016) 2979–2988 (in Chinese).
[18] J. Gao, H.J. Zhang, Two-dimensional joint inversion of seismic velocity and electrical resistivity using seismic travel times and full channel electrical measurements based on alternating cross-gradient structure constraint, Chin J Geophys 59 (11) (2016) 4310–4322 (in Chinese).
[19] N.L. Bennington, H. Zhang, C.H. Thurber, Joint inversion of seismic and magnetotelluric data in the park field region of California using the normalized cross-gradient constraint, Pure Appl Geophys 172 (5) (2015) 1033–1052.
[20] R.Z. Zhang, T.L. Li, 2D data-space joint inversion of MT, gravity, magnetic, and seismic data with cross-gradient constraints, Geophys Prospect 68 (2020) 721–731.
[21] V. Saeed, S. Liu, A.R. Rosemary, X.Y. Hu, et al., An efficient alternating algorithm for the Lp-norm cross-gradient joint inversion of gravity and magnetic data using the 2-D fast fourier transform, IEEE Trans Geosci Rem Sens 60 (2022), 4500416.
[22] Y.G. Li, D.W. Oldenburg, 3-D inversion of magnetic data, Geophysics 61 (2) (1996) 394–408.
[23] Y.G. Li, D.W. Oldenburg, Joint inversion of surface and three-component borehole magnetic data, Geophysics 65 (2) (2000) 540–552.
[24] S. Liu, S. Jin, S. Xuan, X. Liu, Three-dimensional data-space joint inversion of gravity and magnetic data with correlation-analysis constrains, Ann Geophys 65 (2022), https://doi.org/10.4401/ag-8570.
[25] R.Z. Zhang, T.L. Li, Joint MT and gravity inversion using structural constraints: a case study from the Linjiang copper mining area, Jilin, China, Minerals 9 (2019) 407.

Sheng Liu, PhD, Associate professor of Henan University of Urban Construction, China. His interests focused on the exploration of terrestrial planet interior structures using gravity and magnetic field inversion.

Xiangyun Wan, PhD, Associate professor of Henan University of Urban Construction, China. His interests focused on safety production and emergency management.

Shuangggen Jin, PhD, Professor of Shanghai Astronomical Observatory, CAS and Vice-President of Henan Polytechnic University, China. His interests focused on Satellite Navigation, Remote Sensing and Space/Planetary Exploration.

Songbai Xuan, PhD, Associate professor of Shanghai Astronomical Observatory, Chinese Academy of Sciences. His interests focus on interior structures of terrestrial planets using the gravity inversion.

Bing Jia, PhD, Director of the Department of Safety Engineering of Henan University of Urban Construction. He is mainly engaged in the monitoring and early warning research of coal and rock dynamic disasters.

Quan Lou, PhD, Associate professor of Henan University of Urban Construction, China. His interests focused on safety monitoring and early warning, prevention and control of coal and rock dynamic disaster.

Binbin Qin, PhD, Associate professor of Henan University of Urban Construction. His interests focused on safety technology and engineering, underground space engineering.

Rongfu Peng, MD, Teaching assistant of Henan University of Urban Construction, His interests focused on Safety management and technology.

Dali Sun, MD, Assistant Engineer of the First Monitoring and Application Center, CEA. His interest centered on electromagnetic prospecting.